

Journal Pre-proofs

Characterization of dielectric properties and their impact on MAS-DNP NMR applications

Faith J. Scott, Thierry Dubroca, Robert W. Schurko, Stephen Hill, Joanna R. Long, Frédéric Mentink-Vigier

PII: S1090-7807(24)00126-5
DOI: <https://doi.org/10.1016/j.jmr.2024.107742>
Reference: YJMRE 107742

To appear in: *Journal of Magnetic Resonance*

Received Date: 29 March 2024
Revised Date: 17 June 2024
Accepted Date: 13 July 2024

Please cite this article as: F.J. Scott, T. Dubroca, R.W. Schurko, S. Hill, J.R. Long, F. Mentink-Vigier, Characterization of dielectric properties and their impact on MAS-DNP NMR applications, *Journal of Magnetic Resonance* (2024), doi: <https://doi.org/10.1016/j.jmr.2024.107742>

This is a PDF file of an article that has undergone enhancements after acceptance, such as the addition of a cover page and metadata, and formatting for readability, but it is not yet the definitive version of record. This version will undergo additional copyediting, typesetting and review before it is published in its final form, but we are providing this version to give early visibility of the article. Please note that, during the production process, errors may be discovered which could affect the content, and all legal disclaimers that apply to the journal pertain.

© 2024 Published by Elsevier Inc.



Characterization of dielectric properties and their impact on MAS-DNP NMR applications

Faith J. Scott,^a Thierry Dubroca,^a Robert W. Schurko,^{a,b} Stephen Hill,^{a,c}

Joanna R. Long,^{a,d*} Frédéric Mentink-Vigier^{a*}

^aNational High Magnetic Field Laboratory, Florida State University, 1800 E. Paul Dirac Dr., Tallahassee, FL 32310, USA

^bDepartment of Chemistry and Biochemistry, Florida State University, Tallahassee, FL 32306, USA

^cDepartment of Physics, Florida State University, Tallahassee, FL 32306, USA

^dDepartment of Biochemistry and Molecular Biology, University of Florida, PO Box 100245, Gainesville, FL 32610, USA

[*jrlong@mbi.ufl.edu](mailto:jrlong@mbi.ufl.edu), [*fmentink@magnet.fsu.edu](mailto:fmentink@magnet.fsu.edu)

Keywords: Dielectric Properties, Microwaves, Terahertz, Instrumentation, Electron Paramagnetic Resonance, Ceramics, Sample preparation

The dielectric properties of materials play a crucial role in the propagation and absorption of microwave beams employed in Magic Angle Spinning - Dynamic Nuclear Polarization (MAS-DNP) NMR experiments. Despite ongoing optimization efforts in sample preparation, routine MAS-DNP NMR applications often fall short of theoretical sensitivity limits. Offering a different perspective, we report the refractive indices and extinction coefficients of diverse materials used in MAS-DNP NMR experiments, spanning a frequency range from 70 to 960 GHz. Knowledge of their dielectric properties enables the accurate simulation of electron nutation frequencies, thereby guiding the design of more efficient hardware and sample preparation of biological or material samples. This is illustrated experimentally for four different rotor materials (sapphire, yttria-stabilized zirconia (YSZ), aluminum nitride (AlN), and SiAlON ceramics) used for DNP at 395 GHz/¹H 600 MHz. Finally, electromagnetic simulations and state-of-the-art MAS-DNP numerical simulations provide a rational explanation for the observed magnetic field dependence of the enhancement when using nitroxide biradicals, offering insights that will improve MAS-DNP NMR at high magnetic fields.

I. Introduction

Magic Angle Spinning Dynamic Nuclear Polarization (MAS-DNP) combines electron paramagnetic resonance (EPR) with nuclear magnetic resonance (NMR) to enable high sensitivity and high-resolution solid-state NMR experiments. The introduction of commercial MAS-DNP instruments [1–4] operating at *ca.* 100 K has been key to numerous applications to biosolids and advanced materials [5–16].

DNP relies on microwave (μw) irradiation to transfer the higher electron spin polarization originating from paramagnetic species, called *polarizing agents* (PA), to neighboring nuclear spins. Over the past two decades, MAS-DNP sensitivity has improved due to optimization of PAs [17–33], new sample preparation strategies [13,34–38], the introduction of increasingly efficient cooling methods [39–46], and the design of stators for faster spinning [2,3,43,47–49]. Despite these significant efforts, experiments that achieve enhancements near the theoretical limit (*ca.* $658\times$ that of ^1H NMR) remain elusive. Typical experiments show polarization enhancements ranging from 10 to 100 (with respect to thermal equilibrium) [50,51], suggesting ample opportunities for further advancements.

Today’s modern MAS-DNP instruments operate between 4.7 and 21.1 T (^1H Larmor frequencies, $\nu_0(^1\text{H})$, from 200 to 900 MHz) with μw frequencies ranging from *ca.* 100 to 600 GHz [52,53]. Progression to higher magnetic fields is challenging as most MAS-DNP mechanisms have some degree of field dependence; in particular, the most common of these is the cross effect (CE) [21,54]. This field dependence, which is partially explained by theory [54–58], could be counterbalanced with the use of more intense μw irradiation [47,57–61], longer electron spin relaxation times (T_{1e}) [19,24,25,59,62] and increased electron-electron coupling constants for biradicals [21,22]. However, the experimental field dependence of the DNP efficiency for the PA AMUPol in large sample volumes is more drastic than predicted: in 3.2 mm rotors, the enhancement, $\epsilon_{\text{on/off}}$, drops from *ca.* 240 at 9.4 T down to *ca.* 30 at 18.8 T [19,54]. Fortunately, DNP efficiency is better in smaller rotors, *e.g.*, in 1.3 mm rotors, $\epsilon_{\text{on/off}} \approx 60–70$ are obtained at 18.8 T [63]. Some disagreements between theory and experiment support

the hypothesis that μw absorption may be problematic at higher frequencies. In addition, the enhancements from other biradical PAs are largely field independent, which appears, in part, to be to their lower μw power requirements [19,24,62].

Other reports have demonstrated improved enhancement factors by maximizing the average μw magnetic field ($B_{1,e}$), *i.e.*, the electron nutation frequency $\nu_{1,e} = \gamma_e B_{1,e} / 2\pi$. Indeed, having a homogeneous $B_{1,e}$ throughout the sample is highly desirable [48,64–67], since this helps to avoid “inert” and/or overheated sample areas that negatively impact DNP experiments. Higher $\nu_{1,e}$ values can be obtained by: (i) adding dielectric solids to the sample [64,65,68], (ii) changing the rotor wall thickness [40,66], (iii) converting the μw beam from linear to circular polarization [40,43,49,69,70], (iv) reducing μw losses due to RF coil interference [2,48,71,72], and/or (v) designing horns and lenses to focus the μw beam [48,66].

To further improve hardware design, optimize the conditions for the CE mechanism, and refine sample preparation for MAS-DNP at high magnetic fields, we decided to measure the *refractive indices* (n) and *extinction coefficients* (k), to define the dielectric properties of many key materials used in high-frequency EPR and MAS-DNP NMR experiments. At a given frequency, the speed of light in a medium is governed by n , while its opacity is determined by k – both play crucial roles in the propagation of the μw beam which impacts DNP efficiency. Except for liquid water and hexagonal ice, which have highly characterized properties [73], the values of n and k are not known for a broad range of materials used in high-frequency EPR and MAS-DNP NMR. Non-magnetic absorption observed in the μw range arises from the interplay between the electric field generated by the source and the electric dipole moment within the sample. This dipole moment can be induced by μw irradiation or inherent to the molecular system as measured by infrared and rotational spectroscopy. At cryogenic temperatures, vibrational modes—either intramolecular bond vibrations or phonons—predominate. This frequency range is commonly referred to as the THz gap due to a scarcity of available irradiation sources [74]. Consequently, dielectric properties within this range are underdetermined due to the limited availability of such sources.

In this article, we report measurements of n and k from 70 to 960 GHz for a diverse array of liquids, frozen solutions, and solids commonly utilized in MAS-DNP NMR experiments and high-field EPR, by way of a Fabry-Perot interferometer apparatus. Specifically, we characterized the most common sample matrices, including glycerol/water, dimethylsulfoxide (DMSO)/water, 1,1,2,2-tetrachloroethane (TCE), and biological samples at 77 K in their frozen states, as well as ceramics and polymers used in probe components. We then use values of n and k in electromagnetic simulations to improve rotor geometries, optimize electron nutation frequencies, and reduce μw absorption by rotors and samples in MAS-DNP NMR experiments.

Finally, we predict the electron nutation frequencies at different μw frequencies and predict the expected enhancements with numerical simulations. We then discuss the challenges of MAS-DNP NMR at very high magnetic fields (≥ 18.8 T), specifically when using large rotors (*e.g.*, 3.2 mm or larger). We conclude by highlighting the importance of improving sample irradiation for MAS-DNP NMR and, by extension, the application of “pulsed” DNP strategies, which are currently under development for lower fields [75–83].

II. Results

In a MAS-DNP experiment, n impacts the reflective/matching properties at the interface between two media of different refractive indices (n_1, n_2). The reflection coefficient due to the interface, $R_{\text{Interface}}$, is given by:

$$R_{\text{Interface}} = \frac{I_{\text{reflected}}}{I_{\text{incident}}} = \left(\frac{n_1 - n_2}{n_1 + n_2} \right)^2 \quad (1)$$

where I is the μw power that is incident or reflected. Note that eq. (1) is only valid for normal angles of incidence. Significant differences in refractive indices lead to large reflection coefficients. One approach to minimize R when there are multiple interfaces is to adjust the thicknesses of the materials to generate standing waves. They occur when a material with refractive index, n_2 , has a thickness, l_2 , that is a half-

integer multiple (m) of the radiation wavelength in the material, λ_2 :

$$l_2 = \frac{m}{2} \lambda_2 = \frac{m}{2} \frac{c}{n_2 f} \quad (2)$$

where c is the speed of light and f is the frequency.

During irradiation, the attenuation of the μw field and degree of sample warming is determined by the value of k . The absorption can be estimated as:

$$\frac{I_{\text{absorbed}}}{I_{\text{incident}}} = 1 - e^{-\frac{4\pi f k l}{c}} \quad (3)$$

where l is the thickness of the material or sample. For example, with $k = 5 \times 10^{-3}$ and a thickness $l = 2$ mm, *ca.* 4% of the μw power is absorbed at $f = 100$ GHz, while almost 35% is absorbed at 1000 GHz (*i.e.*, an order of magnitude increase in absorption if k remains constant). Increased absorption not only diminishes the average electron nutation frequency but can also elevate the sample temperature.

Both reflection/absorption effects are frequency dependent. This simple analysis underscores the significant impact of frequency increases, emphasizing the need to characterize these quantities for a complete understanding of their influence on DNP.

A. Dielectric measurements on solid and frozen samples

The measured dielectric properties, n and k , for a cross-section of materials at DNP-relevant frequencies are reported in **Table 1**. The measurements for solid samples at room temperature are straightforward, while those for the frozen samples can be more challenging, due to the need to form a homogeneous glass. We note that in some cases, the signal to noise ratio can be too low to reliably extract n and k ; in particular, this is observed in the range of 270-320 GHz, where our μw source generates some artifacts. Furthermore, the main limitations at the highest frequency are the lower power of the source, lower sensitivity of the detector, as well

as higher losses for microwave isolation which reduces the dynamic range of the measurements.

Matrices for MAS-DNP - DNP requires long electron relaxation times ($T_{1,e}$); therefore, to meet this requirement, biradicals are often dispersed in glass-forming matrices at 100 K. Common matrices are divided into two categories: aqueous solvent matrices (e.g., DMSO/water and glycerol/water) and organic solvent matrices (e.g., TCE/methanol mixtures) [84,85]. We measured their dielectric properties, as well as those of their constituents. To validate the accuracy of our instrumentation and modeling approach, we initially characterized ice at liquid nitrogen temperature (77 K) and observed that its refractive index increases slightly from 1.77 to 1.80 over the frequency range from 60 to 960 GHz. The extinction coefficient also increases across the same frequency range. This is in very good agreement with previously reported n values [73,86,87], confirming the robustness of our methods. k value trends are in agreement with reference [86]. However the values in ref. [86] indicate 2×10^{-3} (90 GHz), 6×10^{-3} (245 GHz), 9×10^{-3} (395 GHz), 23×10^{-3} (935 GHz). In general, we found lower k values, 2.6×10^{-3} (220-270 GHz), 4.5×10^{-3} (370-420 GHz), 10×10^{-3} (910-960 GHz). We attribute the lower k to the fact our measurements are carried out at 77 K while the reported measurements in ref [86] are carried out at 266 K. Note that our value at 70-110 GHz suffers from large uncertainty due to the difficulty to fit accurately the dips of the interferogram.

Frozen DMSO has $n \sim 1.86$ and k is essentially constant over the range tested, with a value of *ca.* 10^{-2} . When mixed with water, the n tends to be larger and is not the weighted average of the n values of the two components (unlike in the liquid state [88]).

The behavior of frozen glycerol mirrors that of DMSO, with an n of *ca.* 1.85 that remains essentially constant across all frequencies. A frozen glycerol/water (6/4 v/v%) mixture and frozen DMSO/water (1/9 v/v%)

have similar values of n , with values of k which are the same order of magnitude. Frozen TCE and TCE/MeOH (96/4 v/v%) have n values near 1.67 and are relatively transparent (i.e. $k < 10^{-2}$). MeOH has slightly higher n near 1.73, closer to that of glycerol. MeOH and TCE are observed to have similar extinction coefficients.

Overall, and somewhat expectedly, all common MAS-DNP matrices, including mixtures of glycerol/water (6/4 v/v%), DMSO/water (1/9 v/v%) and TCE/methanol (96:4 v/v%), have moderate k values and are nearly transparent to the μ w beam in their glassy states. It is noted that values for glycerol/water (6/4 v/v%) agree with values reported at 140 GHz [66].

Finally, it is important to note that freezing may induce fractures within the materials, potentially leading to significant scattering of the μ w beam. This, in turn, can diminish the effective μ w field in the sample, as observed via EPR spectroscopy [89].

Biological samples - Frozen egg yolk, egg white, lard, pork, and glucose are included as examples of biological materials with varying lipid, protein, polysaccharide, and water content to mimic samples typically measured using MAS-DNP spectroscopy [7,8,14,90–97]. We chose glucose as a simple representative of carbohydrate materials. More complex natural materials, such as wood, demand a more thorough study due to the variability due to moisture content and other factors such as lignin content, fiber orientation, etc. [98,99]. The values of n are different among these samples but are all below 2 and are, therefore, similar to the solvents. The extinction coefficients of each sample are relatively constant across all the frequency ranges. It is of note that egg yolk is the least transparent of the biological materials tested. Pork loin was cut into slabs with the muscle fibers running parallel to the slab edge (pork parallel) and perpendicular to the edge (pork perpendicular).

Table 1: Dielectric properties (n above and k below) for liquids and solids typically used in DNP experiments (either as part of the sample matrix, the sample rotor, or NMR probe components)

Sample	Temperature (K)	n and ($k \times 10^3$)				
		70-110 GHz	220-270 GHz	270-320 GHz	370-420 GHz	910-960 GHz
Polychlorotrifluoroethylene (Kel-F®)	298		1.50±0.02 3±1	1.50±0.02 3±1	1.50±0.01 3±1	1.50±0.01 4±0.1
		Poly(methyl methacrylate)	298	1.66±0.02 30±10	1.68±0.02 10±1	1.68±0.02 10±1
cross-linked polystyrene (Rexolite®)	298		1.65±0.02 0.5±0.1	-	1.56±0.01 3±0.1	1.59±0.01 1.5±0.1
Sapphire α - Al ₂ O ₃	298	3.15±0.04 1.3±0.6	3.15±0.04 3±1	3.15±0.04 3±1	3.15±0.04 1.3±0.5	3.15±0.04 2.8±0.2
		SiAlON	298	2.86±0.05 3±0.4	2.86±0.05 3±0.4	2.86±0.01 3±0.5
YSZ	298	5.83±0.03 30±10	5.82±0.03 35±3	5.82±0.03 35±3	5.87±0.06 38.1±0.9	-
		Aluminum nitride (AlN)	298	2.92±0.01 6.9±0.1		2.92±0.01 5.1±0.7
H ₂ O	77	1.76±0.01 7±3	1.77±0.1 2.6±0.4	-	1.77±0.02 4.5±1	1.80±0.03 10 ±2
		Dimethyl Sulfoxide (DMSO)	77	1.84±0.01 10.±5	1.87±0.01 10.±2	1.87±0.01 10.±2
DMSO/H ₂ O (1/9 v/v%)	77			1.86±0.05 6±2	1.84±0.05 6±2	1.84±0.05 6±2
DMSO/H ₂ O (6/4 v/v%)	77	1.95±0.01	2.03±0.5	2.03±0.5	2.03±0.1	

Solid materials at room temperature - Common materials used to fabricate NMR rotors such as sapphire crystals, aluminum nitride ceramics (AlN), silicon nitride doped with aluminum oxide ceramics (SiAlON), and yttria-stabilized zirconia ceramics (YSZ), have been characterized (Table 1). Of these, SiAlON and AlN have the lowest refractive indices ($n \approx 2.8 - 2.9$), while $n = 3.15$ for sapphire, in good agreement with the literature [87].

Sapphire, AlN, and SiAlON are considered non-lossy, since k ranges from 1×10^{-3} to 7×10^{-3} . YSZ possess the largest refractive index, with $n \approx 5.8$, and the largest extinction coefficient ($k \approx 35 \times 10^{-3}$). This makes it the most lossy and most reflective material evaluated herein. We note that measurements of dielectric constants at 77 K did not reveal significant changes of n and k for SiAlON and we expect similar behavior for the other rotor materials [100], except for k in YSZ [101].

Common polymers used to make probe parts such as polychlorotrifluoroethylene (Kel-F®), poly(methyl methacrylate) (PMMA), and cross-linked polystyrene (Rexolite®) have nearly constant values of n and k for room temperature measurements across a frequency range of 70 – 960 GHz. We note that some of these materials have been characterized at various frequencies [102–104], which allowed us to verify our method.

B. Designing and testing custom MAS-DNP rotors

Optimizing the rotor wall thickness via numerical simulations – We explored the DNP performance of sapphire, YSZ, AlN, and SiAlON by designing and testing different rotors for MAS DNP.

To maximize the electron nutation frequency, $\nu_{1,e}$, in the active sample volume, we conducted electromagnetic simulations with CST Studio suite, a product of Dassault Systemes (Vélizy-Villacoublay, France). Simulations were conducted to minimize the incident μw reflection by optimizing the rotor wall thickness, using the determined dielectric values and assuming the presence of a frozen glycerol/water (60/40 v/v%) solution in the rotor and an irradiation frequency of 263 or 395 GHz and an input power of 5 W. For each rotor wall thickness, $\nu_{1,e}$ was extracted via a home-

written MATLAB script. As previously reported [64,66], $\nu_{1,e}$ has a very broad distribution within the sample (see Fig. S2) and the average values for each of the four materials are shown in Fig. 1. For each material, an optimal wall thickness corresponds to a half-integer multiple of the wavelength for the μw beam inside the material [40,66]. In addition, $\nu_{1,e}$ increases with the wall thickness, which is attributed to a lens effect from the rotor wall that focuses the μw beam in the sample [40,66].

At 263 GHz, for all rotor materials, the simulations predict $\nu_{1,e}$ to be on the order of 0.2 to 0.50 MHz for 5 W of μw input power (Fig. 1a). The behavior of the average $\nu_{1,e}$ heavily depends on the refractive index of the material. Sapphire, AlN, and SiAlON have similar refractive indices and extinction coefficients ($n \sim 3$ and $k \sim 10^{-3}$). In general, sapphire offers the highest average value of $\nu_{1,e}$ over the entire thickness range. Thus, for a standard rotor wall thickness (0.51 mm), sapphire is both the optimal material and has the near optimal wall thickness. SiAlON and AlN match sapphire's performance for wall thicknesses of *ca.* 0.4 and 0.44 mm, respectively. Beyond these thicknesses, their performance is little worse, eventually surpassing sapphire for thicknesses >0.6 mm.

The case of YSZ, where $n \approx 5.85$ and $k \approx 35 \times 10^{-3}$, differs significantly from the others. Since the refractive index is much larger than the other materials, $\nu_{1,e}$ depends more strongly on the rotor wall thickness, as expected from eqs. 1 and 2. The average value of $\nu_{1,e}$ ranges between 0.18 MHz (*ca.* 0.44 mm) and 0.37 MHz (*ca.* 0.51 mm) and is much lower than for other ceramics. For thin walls (0.3 mm), the YSZ rotors have values of $\nu_{1,e}$ similar to sapphire. This agrees with experimental observations that thin wall YSZ rotors perform well on a 400 MHz / 263 GHz DNP instrument. As the wall thickness increases, the average $\nu_{1,e}$ in YSZ has a strong dependence on wall thickness, which is due to the interference/resonances induced by the slab [40], and optimal transmission can be found at *ca.* 0.38 and 0.51 mm.

At a higher μw frequency of 395 GHz, the simulations predict slightly lower nutation frequencies overall (Fig. 1b). The largest values of $\nu_{1,e}$ are obtained for AlN, sapphire, and SiAlON, with the lowest observed for YSZ, irrespective of the wall thickness. For the first three materials, changing the wall thickness

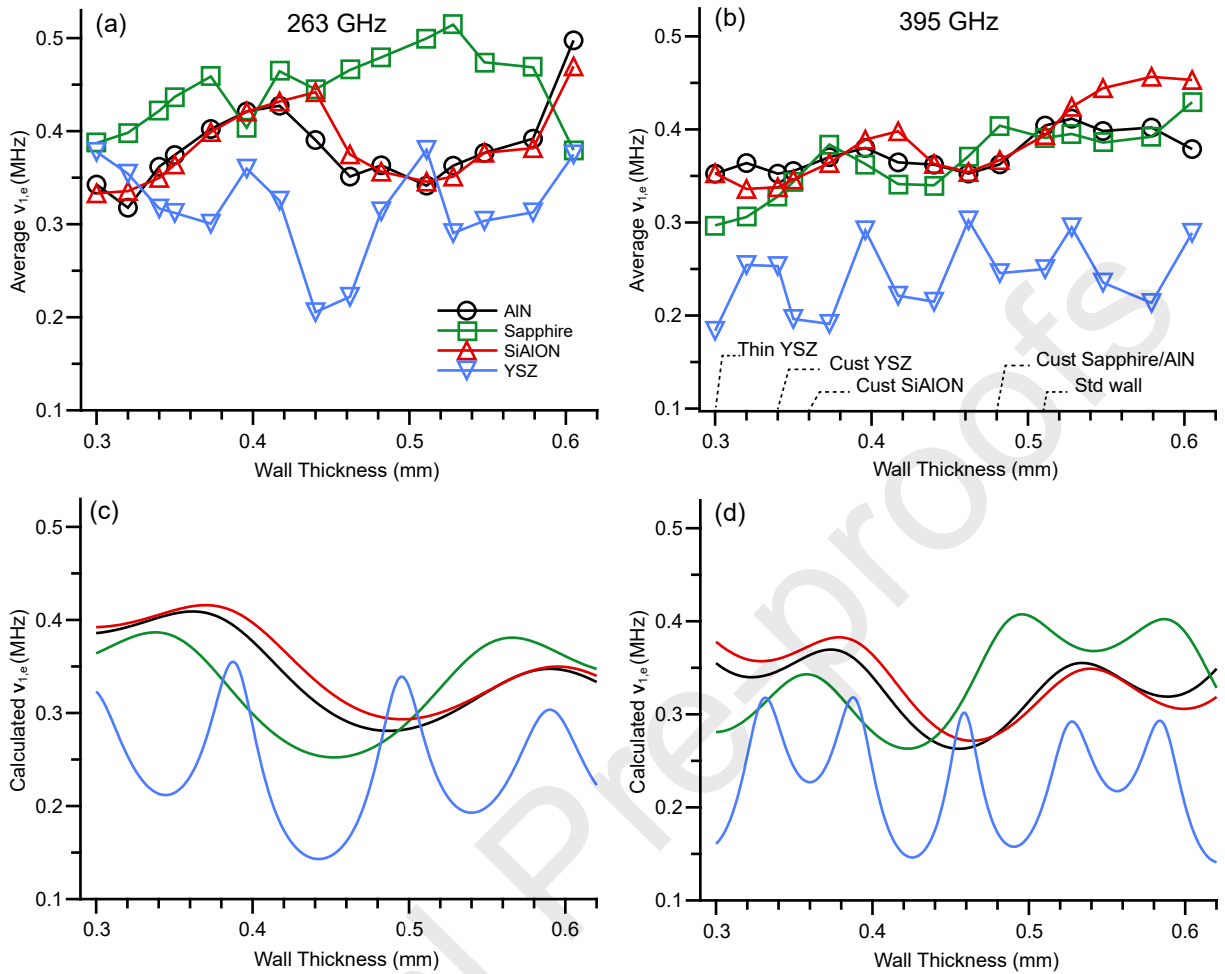


Fig. 1: (a,b) Average electron nutation frequency, $\nu_{1,e}$, plotted as a function of wall thickness at μW irradiation frequencies of (a) 263 GHz and (b) 395 GHz, as simulated in CST Studio assuming 5 W of μW input power and a gaussian beam waist (*i.e.*, irradiance is $\propto 1/e^2$ of the maximum) of 3.2 mm, to mimic the presence of a lens. Sample: glycerol/water (6/4 v/v%) glass, rotor materials as labeled. Reported nutation frequencies are for a linearly polarized beam. (c,d) Calculated electron nutation frequency, $\nu_{1,e}^{calc}$, from the waveguide output to the center of a rotor using eq. (7). See text for details.

only induces a change in the nutation field of *ca.* 10%. The highest $\nu_{1,e}$ reaches *ca.* 0.4-0.45 MHz for AlN, sapphire, and SiAlON. This value is in good agreement with previous reports in sapphire [51,67]. The average $\nu_{1,e}$ in YSZ is even more strongly dependent on the rotor wall thickness and, on average, significantly lower than for the other materials: the optimal value of $\nu_{1,e}$ is 0.29 MHz for rotor wall thicknesses of 0.39, 0.46 and 0.53 mm; this decreases to 0.18 MHz for 0.3 mm.

Optimizing the rotor wall thickness via an analytical model - The utilization of finite element simulations with CST is necessary to obtain accurate nutation frequencies. However, as the μW frequency increases, simulations become very time-consuming. For example, it takes multiple days to simulate with a 527 GHz μW beam impinging on a 3.2 mm YSZ rotor. Thus, we devised a simpler approach to obtain the optimal wall thickness at various frequencies. The transmission with respect to the wall thickness can be calculated using the matrix for a transmission line [105,106]. The transmission coefficient, T , is given by:

$$T = \left| \frac{2}{A + B + C + D} \right|^2, \quad (4)$$

where A , B , C , and D are obtained using the matrix for a transmission line M [87]. This matrix for a simple slab of thickness l and dielectric constants n and k is:

$$M = \begin{pmatrix} A & B \\ C & D \end{pmatrix} = \begin{pmatrix} \cosh \gamma l & Z \sinh \gamma l \\ \frac{1}{Z} \sinh \gamma l & \cosh \gamma l \end{pmatrix} \quad (5)$$

where $Z = 1/(n - ik)$ is the characteristic impedance normalized with respect to the impedance of free space, and $\gamma = \frac{2\pi}{\lambda_0}(k + in)$ with λ_0 as the wavelength of the beam in free space [106,107]. If the beam goes across two slabs, the matrix becomes:

$$M = \begin{pmatrix} A & B \\ C & D \end{pmatrix} = \begin{pmatrix} A_2 & B_2 \\ C_2 & D_2 \end{pmatrix} \begin{pmatrix} A_1 & B_1 \\ C_1 & D_1 \end{pmatrix} \quad (6)$$

In our case, indices 1 and 2 refer to the rotor and sample, respectively. To find the optimal rotor wall thickness, one calculates the μw power transmitted through a slab of rotor material followed by a slab of the sample while keeping the total thickness equal to 1.6 mm (half of the 3.2 mm rotor diameter), *i.e.*, $l_1 + l_2 = 1.6$ mm.

From the transmission coefficient, T , we can predict the nutation frequency, $\nu_{1,e}^{\text{calc}}$, in the sample. If we assume that full transmission of the μw beam, *i.e.*, $T = 1$, leads to a nutation in the sample of $\nu_{1,e,0}$, we have:

$$\begin{aligned} \nu_{1,e}^{\text{calc}} &= \nu_{1,e,0} \sqrt{T} \\ &= \nu_{1,e,0} \left| \frac{2}{A + B + C + D} \right|, \end{aligned} \quad (7)$$

To have a good agreement between the CST simulation and the model we chose a scaling factor $\nu_{1,e,0} = 0.45$ MHz. The results are plotted for each material at both frequencies in **Fig. 1(c)** and **1(d)**. The general shapes of the plots of $\nu_{1,e}^{\text{calc}}$ are similar to the nutations predicted by CST. The model provides close to quantitative

agreement with results obtained with CST. However, it fails for larger wall thicknesses, since the curvature of the rotor wall and effect of the other half of the rotor is not considered in the model. The plots of $\nu_{1,e}^{\text{calc}}$ as a function of wall thickness indicate that thicker walls appear to generate a lens/mirror effect that increases $\nu_{1,e}$. This is observed in **Fig. S1**, but the exact details are beyond the scope of this article. We note that the model does not accurately capture the behavior of the sapphire rotors at 263 GHz, which may arise from the convexity of the rotor wall (**Fig. S1**).

All in all, this analytical model enables easy computation of the expected values of $\nu_{1,e}$ at low computational expense, enabling studies of the effects of the μw frequency, as well as the impacts of the rotor contents and wall thickness on the optimal values of $\nu_{1,e}$. Further examples are given in **Fig. S3**.

Testing the rotors for MAS-DNP: Enhancement and volume-adjusted sensitivity at 395 GHz - To verify some of the predictions made with the CST simulations, we designed and tested several rotors made of the aforementioned materials and tested them under 600 MHz/395 GHz MAS-DNP conditions. Seven rotors were tested, including two commercial rotors (standard wall sapphire and YSZ from Bruker), and five custom-made rotors by O'Keefe Ceramics (Colorado, USA). We evaluated their performances in term of signal enhancement and volume-adjusted sensitivity, *i.e.*, taking the sample volume into account (**Table 2**). The optimal μw power for each material was determined by dialing power down with an attenuation grid on the 600 MHz / 395 GHz MAS-DNP instrument [70] (**Fig. 2**). At the time of machining, only the sapphire and YSZ rotors had the optimal wall thicknesses.

Table 2 Maximum enhancements observed for ^{13}C -proline with 10 mM AMUPol using different rotors. All rotors have the same outer diameter (3.2 mm).

Rotor material	Wall thickness (mm)	Relative volume, R_v	$\epsilon_{\text{on/off}}$	$\epsilon_{\text{on/off}} \times R_v$
Std. sapphire (Bruker)	0.51	1	170 ± 10	170 ± 10
Cust. Sapphire	0.48	1.14	170 ± 10	194 ± 11
Thin wall YSZ	0.30	1.41	91 ± 5	128 ± 7
Cust. YSZ	0.34	1.42	125 ± 5	178 ± 14
Std. YSZ (Bruker)	0.51	1	90 ± 5	90 ± 5
Std. SiAlON*	0.51	1	$157^* \pm 5$	$157^* \pm 5$
Cust. SiAlON	0.35	1.40	141 ± 5	197 ± 14
Cust. AlN	0.48	1.12	148 ± 5	166 ± 11

*The MAS-DNP experiments were conducted on the same probe with the same solution for all rotors except for the SiAlON rotor with a wall thickness of 0.51 mm. This rotor was tested on another probe with a new batch of solution. Therefore, measurements were performed on the same probe and on the new solution in the standard sapphire rotor (0.51 mm), $\epsilon_{\text{on/off}} = 152$. The enhancements obtained with the SiAlON rotor (0.51 mm) were scaled to enable the comparison with the other rotors.

The sapphire rotors, either standard or custom wall, provide the highest $\epsilon_{\text{on/off}}$, with an average enhancement of *ca.* 170 ± 10 , as previously reported [51]. This is in line with the prediction that indicated the

minimal impact of the wall thickness on $\nu_{1,e}$ (Fig. 1). For these samples, we observed a large uncertainty in $\epsilon_{\text{on/off}}$ and both rotors appear to be equivalent within experimental uncertainty ($\sim 5\%$). We did observe variations in enhancements and believe that it is related to the formation of a bubble (~ 1 mm diameter) that appears to affect the MAS-DNP efficiency but cannot easily be reproduced.

Experiments using the commercial thin wall YSZ (0.3 mm) and custom wall (0.34 mm) rotors had the lowest enhancements, with $\epsilon_{\text{on/off}}$ of 91 ± 5 and 125 ± 5 , respectively. This again matches our predictions, since $\nu_{1,e}$ is expected to be lower (0.18 vs. 0.25 MHz). We note that the experiments using rotors with the slightly thicker custom walls (0.34 mm) performed significantly better than those employing both the thin and standard walls. The commercial Bruker standard wall rotor (0.51 mm) has a predicted $\nu_{1,e} = 0.22$ MHz, as corroborated by a smaller $\epsilon_{\text{on/off}}$ of 90 ± 5 .

MAS-DNP experiments using a custom AlN rotor with a 0.48 mm wall thickness (same as the optimal sapphire thickness to find matching rotor caps), performed very well, with a maximum $\epsilon_{\text{on/off}} = 148 \pm 5$.

Finally, two SiAlON rotors were assessed, one with a wall thickness concurrent with the Bruker standard (0.51 mm) and one with a “custom” thinner wall (0.35 mm). (The latter was designed to maximize sample volume while maintaining mechanical stiffness [108]). Values of $\epsilon_{\text{on/off}}$ of 157 and 141 were obtained, respectively. While the 0.35 mm walled rotor does not have the optimal wall thickness for maximum transmission (according to the simulations), experiments confirm the predictions: experiments with SiAlON rotors are superior in performance to those employing YSZ rotors with an optimal wall thickness of 0.34 mm. This suggests that SiAlON rotors could be made with thinner walls (e.g. 0.42 mm) to maximize the sample volume without sacrificing the DNP performance, unlike the case of YSZ rotors.

In summary, sapphire, AlN, and SiAlON are acceptable materials for MAS-DNP NMR at 395 GHz. Notably, changing the wall thickness of rotors made from these materials does not significantly impact the performance. On the opposite, YSZ is not a good material for a 3.2 mm rotor at 395 GHz, as all the

experiments led to the lowest enhancements, even for the rotors with optimal wall thicknesses. AlN is rather brittle, hence using thinner walls may not be recommended.

In accounting for the relative sample volume, R_v , of each rotor, it is observed that DNP experiments using custom sapphire, custom YSZ, and custom SiAlON rotors offer the best signal intensities, with effective sensitivity gains, $\epsilon_{\text{on/off}} \times R_v$, of ~ 180 -200. All other custom rotors offer performance within 10% of commercially available sapphire rotors, with SiAlON being the best alternative rotor material at 395 GHz. Sapphire remains the best rotor material in terms of absolute enhancement, but the performance of SiAlON in terms of sensitivity and mechanical resistance is worth exploring, since this stronger material supports the creation of rotors with thinner walls and larger sample volumes.

Testing the rotors for MAS-DNP: Power dependence analysis at 395 GHz - Beyond the comparisons of direct enhancements, the incident μw power was varied to assess the power dependence of the enhancement for each type of rotor. This relates to the ability of the material to deliver μw power to the sample and dissipate heat. The DNP efficiency, and therefore enhancement, improves with decreasing temperature.

Experimental enhancements as a function of the μw input power as shown in Fig. 2. Sapphire, AlN, and SiAlON rotors lead to similar dependences and the optimal enhancements are obtained with an input μw power at the probe base of *ca.* 10 W. All these materials enable good sample irradiation, heat dissipation, and low absorption at 395 GHz, $k \approx 1.8 \times 10^{-3} - 5.1 \times 10^{-3}$. SiAlON, has a thermal conductivity of 12-25 $\text{Wm}^{-1}\text{K}^{-1}$ at 300 K, while sapphire has a thermal conductivity of 190 $\text{W m}^{-1} \text{K}^{-1}$ at 100 K, and AlN's is 170-220 $\text{Wm}^{-1}\text{K}^{-1}$ at 290 K) [109–112]. The better DNP performance of sapphire rotors may be due to both their higher thermal conductivity and low absorption coefficients.

The experiments with the YSZ rotors exhibit the lowest enhancements at all μw powers, even in the case of optimized wall thickness, with a low optimal input μw power of *ca.* 7-10 W. Beyond 10 W, the enhancements decrease significantly in comparison to

the other materials. This decrease is caused by sample heating [64], illustrating the increased μw absorption and generating heat. Indeed, due to the large n , most of the μw power tends to be contained within the rotor wall (Fig. S1), while the larger k leads to significant absorption. The sample heating is significant, and we observe that the ^1H NMR spectra show two peaks: one broad and one narrow. The narrow peak is indicative of the liquid state arising from sample melting. The DNP enhancements in these rotors thus decrease at high μw input powers. YSZ has low thermal conductivity (1.8-2.9 $\text{W m}^{-1} \text{K}^{-1}$) in comparison to sapphire (thermal conductivity 190 $\text{W m}^{-1} \text{K}^{-1}$) [109,110,113]; therefore, samples in YSZ rotors tend to melt at lower μw powers than those in sapphire rotors.

The thin-walled YSZ rotor exhibits different behavior: no sample melting is observed. Instead, even using a μw power of 13 W at the probe base, the enhancement does not reach a plateau. This indicates that the actual μw field in the sample is low and, based on the transmission calculation, a significant portion of the μw beam is reflected by the rotor's walls.

In summary, these experiments confirm the findings from the CST studio suite simulations: sapphire, AlN, and SiAlON are good choices of materials for 3.2 mm MAS-DNP rotors at 395 GHz. Conversely, for 3.2 mm rotors, YSZ should be avoided at 395 GHz.

C. MAS-DNP at high field.

A long-standing debate exists in the MAS-DNP community about the magnetic field dependence of the cross effect. Early literature reports that the enhancement obtained with the cross-effect mechanism has a $1/B_0$ dependence on magnetic field, B_0 [114], while subsequent work claims a scaling proportional to $1/B_0^2$ [54]. Both are in contradiction with other theoretical predictions [57–59,62]. However, the experimental observations also contradict the simulations. We believe that some of the observed trends can be attributed to the rotor and sample absorbing the μw beam, which could be responsible for the reduction of enhancement at high field.

In Fig. 3(a) we report the simulated values of $\nu_{1,e}$, using CST studio suite for different rotor materials and

μW frequencies. In standard sapphire rotors, the nutation drops from 0.46 to 0.30 MHz as the μW frequency increases from 263 GHz to 527 GHz. With knowledge of the $\nu_{1,e}$ values, we can attempt to quantitatively simulate the enhancement using a previously published method [23,51,115]. The results are reported in Fig. 3(b).

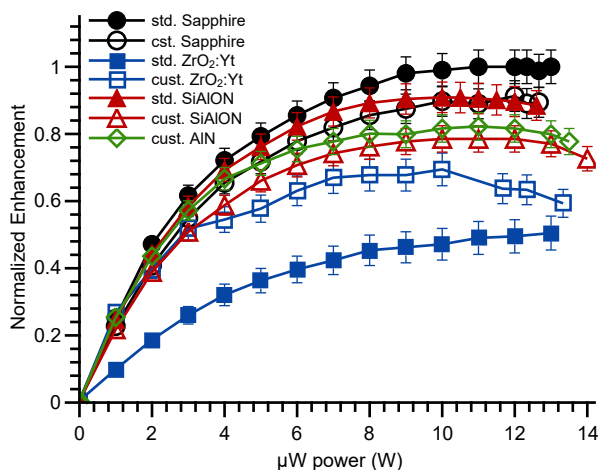


Fig. 2 Normalized DNP enhancement (signal μW on/signal μW off) as a function of μW power for a sample of 250 mM proline with 10 mM AMUPol in 6:3:1 glycerol- d_8 /D₂O/H₂O using different rotors. Full and open symbols correspond to standard or custom wall thickness.

The simulations capture the qualitative nutation behavior as a function of the μW frequency/magnetic field. The enhancement, $\epsilon_{\text{on/off}}$, decreases with the μW frequency/magnetic field and the simulations provide quantitative agreement at 263 and 395 GHz (with an overestimation of *ca.* 15%). At 527 GHz, the experiment and simulation is not as quantitative. The latter still predicts a decrease in enhancement with increase in μW frequency, but still overestimates the enhancement by a factor ranging from 2 to 3.

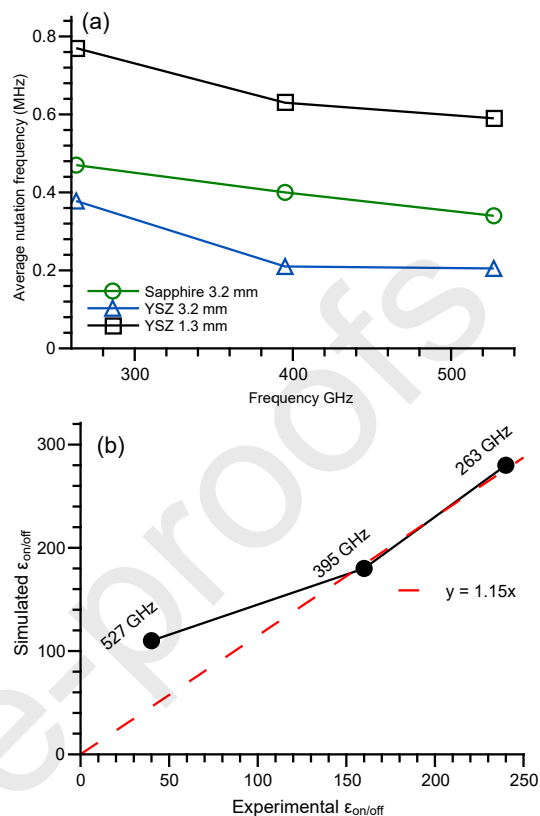


Fig. 3 (a) Simulated average electron spin nutation frequencies as a function of μW irradiation frequency for a 3.2 mm sapphire rotor (green circle), a 3.2 mm thin-wall YSZ rotor (blue triangle), a 1.3 mm YSZ rotor (black squares). In all cases, 5 W input linearly polarized irradiation and rotors filled with glycerol/water (6/4 v/v%) were assumed. (b) simulated enhancement using a prior MAS-DNP model [23,51,115] for a 3.2 mm sapphire rotor containing 10 mM AMUPol in glycerol- d_8 /D₂O/H₂O (6/3/1 v/v/v%) assuming the calculated nutation behavior shown in (a).

All in all, the simulations confirm that lower μW nutation frequency can be responsible for the reduction of DNP efficiency at higher fields. The disagreement at 527 GHz can be explained by taking into account additional factors such as:

1. The simulations overestimate $\nu_{1,e}$ in the sample, as the NMR radio-frequency coil is not taken into account in the EM simulations;

2. The electron relaxation times, $T_{1,e}$, are assumed constant for all simulations – however, they may be shorter at high field;
3. The effect of sample heating is ignored in the simulations. However, they would impact the $T_{1,e}$'s and k which is likely to increase with temperature (particularly if a phase transition occurs), thus the $\nu_{1,e}$ which would be reduced.

Testing these hypotheses is outside the scope of this work.

We conducted additional EM simulations using CST studio suite for YSZ 3.2 mm thin wall and 1.3 mm standard rotors. Again, $\nu_{1,e}$ drops significantly at higher fields for the 3.2 mm rotor, whereas the drop is significantly less for the 1.3 mm rotor. This is reinforced by experimental results that show better performance for AMUPol in 1.3 mm rotors at 527 GHz [63]. Note that the MAS-DNP simulation tool was not used, since the presence of the coil was ignored; it is very likely that experimental nutation frequencies are lower if the coil interferes with the μw beam [48].

Small rotors combine multiple advantages for high field MAS-DNP: (i) since the μw beam radial power distribution is gaussian [87], the highest power density is in the center (Fig. 4) which leads to a higher and more homogeneous $\nu_{1,e}$; (ii) smaller rotors allow better heat dissipation, thus keeping the sample cooler, which in turn ensures longer $T_{1,e}$ s; (iii) the amount of μw absorption by the sample is inherently lower due to the shorter path length. In a nutshell, the surface to volume ratio favors better heat dissipation in smaller rotors.

However, it should be noted that due to Malus' law, the acceptance angle for the μw beam narrows as the index of refraction is increased (see schematic in Fig. 4). Thus, for high- n materials such as YSZ, the μw power that reaches the sample should be lower. Instead, materials with lower refractive indices should be favored for small rotors.

All in all, these results point to the observed field dependence being due to changes in $\nu_{1,e}$ at high fields, especially for bis-nitroxides. Unfortunately, in a sample that absorbs μw , increasing the irradiation power may not improve the efficiency of the DNP as higher μw power lead to an increased sample temperature, which in turn can lead to shorter relaxation times that reduce

the enhancement (as observed in the custom YSZ rotors in Fig. 2). As pointed out in the introduction, recent hetero-biradicals, such as TEMTRiPol-I [19], PyrroTriPol [24], or HyTEK-2 [25], show very good performance at all fields – this could be explained by their lower μw power requirements.

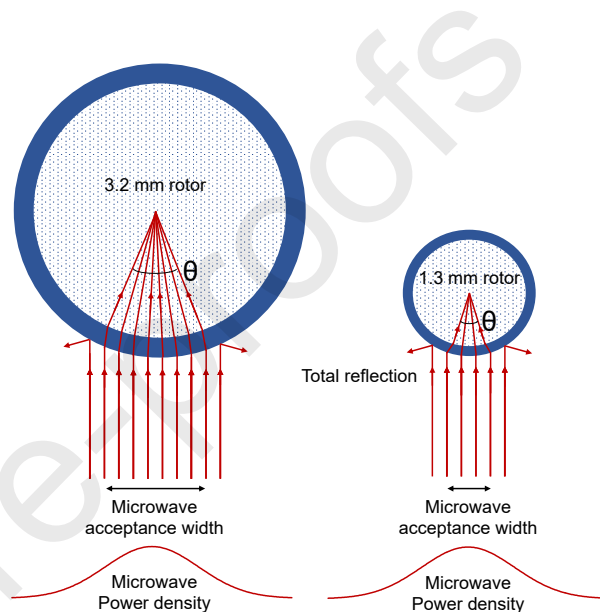


Fig. 4 Schematic of μw irradiation of rotors of different sizes. θ denotes the acceptance angle of the incident beam. Outside of that angle the μw are reflected by the external surface of the rotor.

Lastly, we draw the reader's attention to the fact $\epsilon_{\text{on/off}}$ does not provide quantification of the performance of the cross effect [55,116]. Indeed $\epsilon_{\text{on/off}}$ includes the effect of the nuclear depolarization in the case of AMUPol [51,55]. The decrease of $\epsilon_{\text{on/off}}$ at higher μw frequencies is also due to a reduction of the depolarization effect, as previously discussed [51,55]. When considering the polarization gain, which quantifies the cross-effect performance, the ratio of the signal intensity with μw compared to the thermal equilibrium signals, ϵ_B (see SI for definition), does not drop as abruptly as shown in Fig. S4.

III. Discussion and conclusions

In this article, we present measurements of dielectric properties for key materials and matrices used in high field DNP and EPR. Many of the dielectric properties, particularly those of solvents and biological matrices, have not been previously reported within the frequency range of 70-960 GHz. Using a distinctive instrumentation approach based on quasi-optic principles, we developed a method enabling the extraction of dielectric properties at liquid nitrogen temperatures.

Across the entire frequency range, refractive indices remain nearly constant, with some observed variations in the extinction coefficients. As expected, all materials and matrices prove to be transparent in this frequency range. While the extinction coefficients remain consistent, their influences become more pronounced at higher frequencies. Consequently, materials and matrices that absorb μw radiation to some degree may prove impractical for high-field/high-frequency DNP. As a general guideline, k appears to correlate with the polarity of the chemical structure as previously reported [117] and thus samples with larger k are challenging for high field MAS-DNP. For instance, glass matrices such as DMSO/H₂O, where DMSO constitutes a sizable portion, exhibit higher absorption, as does PMMA in comparison to polypropylene. Therefore, these matrices and materials are not advised for use in high-field DNP experiments. In practice, mixtures of DMSO-*d*₆/D₂O/H₂O (6/3/1 v/v/v%) serve as reasonable matrices at 263 GHz, while sample melting can be observed at 395 GHz if the maximum available μw power is used. The dielectric measurements conducted here offer valuable insights to guide sample preparation for high-field DNP experiments.

The knowledge of dielectric properties is necessary to develop new hardware for high field DNP. Using the measured dielectric properties, we have been able to design new rotors to conduct DNP experiments at 395 GHz. EM simulations enabled us to determine the nutation frequencies that are in good agreement with empirically determined values [50,51]. These were complemented by a simpler model that allows for the quick determination of the optimal rotor wall thickness for a given rotor material and sample content. This simple model can be used at any frequency and could be used to predict the optimal wall thickness for future 1.2 GHz MAS-DNP NMR instruments. It can also be

used to tailor rotors for specific applications, *e.g.*, samples with very large refractive indices such as oxides (an example is shown in **Fig. S3**).

Sapphire, AlN, and SiAlON exhibit lower refractive indices and lower absorption compared to conventional YSZ rotor materials, with sapphire standing out as the optimal choice due to its high thermal conductivity, making it particularly well-suited for DNP applications. On the contrary, conventional YSZ has unfavorable properties for high-field DNP. Despite its strength, YSZ's high n contributes to increased reflection, while its high k leads to increased μw absorption. Its limited thermal conductivity also makes it less suitable, especially at 395 GHz and potentially at higher frequencies.

SiAlON emerges as a favorable alternative to YSZ. Although it has a lower tensile strength, T (400-700 MPa vs. 500-750 MPa for YSZ), it boasts a lower density ($\rho \approx 3$ vs. 6 g cm⁻³); thus, the two materials have similar maximal spinning frequency, $\nu_r^{\text{max}} \propto \sqrt{(T/\rho)}$ [108]. Meanwhile, SiAlON has similar dielectric properties to sapphire, making it attractive for high-field DNP applications. We also note that Si₃N₄, a very stiff material, has been successfully employed in very low-temperature DNP scenarios [45,118] and could also be of interest; however, it is challenging to machine in comparison to SiAlON.

Finally, our understanding of dielectric properties has provided crucial insights into high-field DNP and the observed trends in the underlying mechanisms. Generally, the μw field diminishes at higher fields due to increased absorption, especially in larger rotors. Although higher μw power could potentially compensate for this effect, it would simultaneously raise the temperature, leading to faster $T_{1\rho}$ s, which result in reduced DNP efficiency. Hence, the optimization of DNP efficiency at high fields requires a delicate balance between mitigating absorption-related losses and managing the associated increases in temperature. Achieving this balance is essential for advancing the efficacy of high-field DNP applications. It is expected that as long as DNP instruments use cold N₂ at ~ 100 K, this balance can only be obtained with small rotors at high fields. We anticipate that larger rotors will work effectively at high fields with lower temperature MAS-DNP instrumentation [46,118].

One important material for rotors was not characterized in this work, namely, diamond, due to cost limitations. Diamond exhibits the best properties in all the aforementioned categories for improvement of DNP enhancement. It has a relatively low $n \sim 2.4$ and low $k \sim 0.001$ [87] at relevant frequencies 200 – 1000 GHz, as well as a very high thermal conductivity ($13000 \text{ W m}^{-1} \text{ K}^{-1}$ at 100 K) [109,119,120], which is several orders of magnitude higher than that of sapphire, allowing for more efficient sample cooling. Finally, its high tensile strength and low density permits higher MAS rates. It is noted that rotors designed from diamond material are still in the development phase, due to high costs and challenges in machining, but recent results offer promising prospects [109].

IV. Materials and Methods

Dielectric measurements

n and k are extracted from the interference pattern generated by a Fabry-Perot interferometer [106,121]. Here, we use a broadband quasi-optical (QO) system [87] with appropriate sources for each frequency range (**Fig. 5**), allowing measurements on liquids, solids, and frozen samples. To cover the frequency range of interest to DNP (100-600 GHz), four different μw source/receiver combinations were used, each covering the following bands: 70-120 GHz, 220-320 GHz, 370-420 GHz, and 910-960 GHz. The sources and mixers (*i.e.*, detectors) are controlled by a Keysight Network Analyzer model N5222B combined with either AB Millimetre or Virginia Diodes Inc. frequency multipliers to reach the desired frequency band.

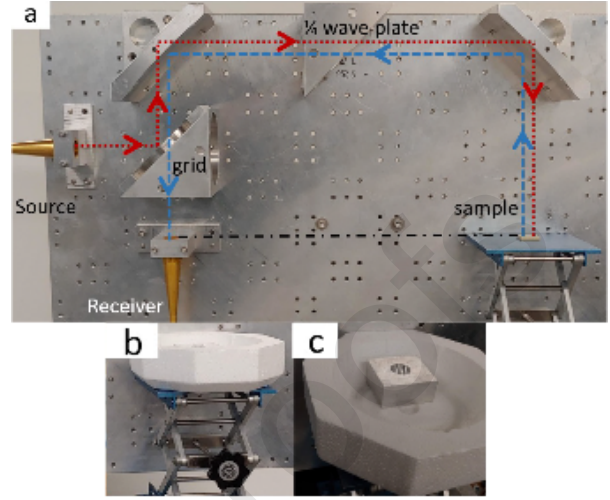


Fig. 5 (a) Photograph of the dielectric measurement interferometer. The QO bench is oriented vertically such that the μw beam interacts with the samples from the free surface. The dotted/dashed lines indicate the incident (red) and reflected (blue) μw beam paths. The black dash-dot line shows that the top surface of the sample and the receiver horn aperture are in the same plane. This system supports measurements of (b) solids and (c) frozen liquids using an aluminum cup cooled with liquid nitrogen.

The QO bench is designed to direct the μw beam from the source to the sample and back toward the receiver via a series of refocusing mirrors. The beam exiting from the source (**Fig. 5(a)**, red dotted lines) is linearly polarized, and first meets a wire grid oriented with respect to it as a mirror. After reflection, the beam then travels through space and through a $1/4$ wave plate, which rotates the polarization by 45° . The beam then travels to the sample and is reflected. This reflected beam (**Fig. 5(a)**, blue dotted line) is thus rotated once again by 45° before traveling through the grid, which is transparent for this polarization angle ($+90^\circ$) before reaching the receiver. The polarization of the μw beam

$$\log(R) = 2 \log\left(\frac{I_0 - I}{I_0}\right)$$

$$= 2 \log\left(\frac{\left(n - ik - \frac{1}{n - ik}\right) \sinh\left[\frac{\pi(4nl - \lambda_0)}{2\lambda_0}(k + in)\right]}{2 \cosh\left[\frac{\pi(4nl - \lambda_0)}{2\lambda_0}(k + in)\right] + \left(n - ik + \frac{1}{n - ik}\right) \sinh\left[\frac{\pi(4nl - \lambda_0)}{2\lambda_0}(k + in)\right]}\right) \quad (8)$$

ensures isolation between the forward and return μw beam paths. Using a vector network analyzer, the collected signal is normalized to a reference spectrum, such that it produces the reflection coefficient (R). The reflection spectrum is then fitted using equation (8) to extract n and k [106].

Examples of interference patterns are shown in **Fig. 6**. The periodicity of the interference patterns relates to n and the thickness of the sample, l , while the amplitudes of the oscillations are related to k .

The interferometer can be used to characterize solid samples at room or low temperatures (in principle, liquids also). To form a Fabry-Perot resonator, the samples must have flat surfaces on both sides that are parallel to one another, thus leading to internal reflections and a quality factor, $Q > 1$. To this end, the solid samples characterized at room temperature were precisely machined. For frozen samples, such as DNP matrices (*e.g.*, glycerol-water) at 77 K, the solutions were poured into an aluminum cup that was subsequently partially immersed in liquid nitrogen inside of a larger insulated bowl (**Fig. 5(c)**). To produce a flat frozen surface, additional sample was added to yield a domed surface, then a room-temperature aluminum plate was applied. The plate was then removed to measure the sample's properties. Note that solutions must be degassed by freeze-thaw cycles to reduce internal cracking and obtain a precise interferogram (without scattering). Multiple thicknesses (**Table 3**) were measured whenever possible, especially in the case of challenging samples, so that more potential interferograms were available in the fitting step.

Table 3 Thicknesses of each sample studied.

Sample	Thickness studied (mm)
Polychlorotrifluoroethylene (Kel-F®)	6.5, 13.3, 20, 26.5
Poly(methyl methacrylate)	11.4
cross-linked polystyrene (Rexolite®)	9.4, 19.3
Sapphire α – Al ₂ O ₃	3.4, 5, 6.1, 12.1
SiAlON	7.5, 10.2, 12.7
YSZ	4.02, 5.07
Aluminum nitride (AlN)	6.9, 10.4, 13.9
H ₂ O	5.5, 11.4, 18.2
Dimethyl Sulfoxide (DMSO)	5.5, 11.4, 18.2
DMSO/H ₂ O (1/9 v/v%)	5.5, 11.4, 18.2
DMSO/H ₂ O (6/4 v/v%)	5.5, 11.4, 18.2
Glycerol	5.5, 11.4, 18.2
Glycerol/H ₂ O (1/9 v/v%)	5.5, 11.4, 18.2
Glycerol/H ₂ O (6/4 v/v%)	5.5, 11.4, 18.2
1,1,2,2-tetrachloroethane (TCE)	5.5, 11.4, 18.2
Methanol (MeOH)	5.5, 11.4, 18.2

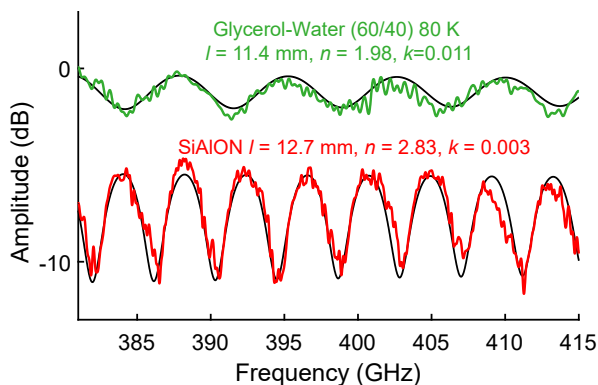


Fig. 6 Reflection interferogram for SiAlON (red line) and a frozen glycerol-water mixture (green line), and their respective best fits to eq. (8) (black traces). The SiAlON interferogram was acquired at room temperature with a $l = 12.7$ mm thick sample. The glycerol-water mixture interferogram was acquired at 80 K with a $l = 11.4$ mm thick sample. The n and k values used to fit the curves are shown for each trace. Interferogram curves are vertically shifted for clarity.

Fitting and error extraction

TCE/MeOH (96/4 v/v%)	5.5, 11.4, 18.2
Egg white	3.0, 6.2, 16.0
Egg yolk	5.8, 17.7
Lard	4.1, 8.1, 14.5
Pork parallel	7.2, 12.7
Pork perpendicular	9.6, 15.3
Glucose/Water (1/1 w/w%)	5.5, 11.4, 18.2

Glucose/Water (2/1 w/w%)

5.5, 11.4, 18.2

Egg and pork-derived samples, serving as protein and lipid analogs to biomaterials studied by DNP, were allowed to freeze slowly in a -20°C freezer to avoid crack formation before being measured in a liquid nitrogen bath. Generally, the absorption is relatively high ($k \approx 0.01$) for these samples; thus, the sample thickness was reduced to observe clear interference patterns and accurately measure n and k . Lean pork loin samples were cut and pressed to produce flat, uniform top and bottom surfaces before being frozen.

MATLAB (Mathworks, Natick MA) was used to automate the fits using eq. (8), where R is the normalized reflection coefficient, I_0 is the intensity of the reflected signal in the presence of a reference mirror at the location of the sample, I is the intensity of reflected signal in the presence of the sample, l is the thickness of the sample, and λ_0 is the wavelength of the μw radiation in free space. Note that eq. (8) assumes the presence of a perfect mirror below the sample (reflectivity of 1), and in the case of frozen solutions, the mirror is made of the sample cup (see SI for derivation). Whenever possible, n was extracted on thicker samples to obtain a higher precision fit. To determine k , we chose the thickness that leads to the best fit. (this value changes for each frequency range).

Experimental data were fit using MATLAB (MathWorks Inc., USA) script to extract n and k using equation (8). A four-step iterative fitting process was used to determine dielectric properties and their errors. An initial guessed refraction index, n_{ini} , is obtained based on the periodicity of the interference pattern over the measured frequency range. Using n_{ini} , a fit of the initial k value to the experimental data using the Levenberg-Marquardt algorithm. If this algorithm does not converge, the index of refraction is randomly varied (i.e., n selected in the interval $[0.9, 1.1] \times n_{\text{ini}}$). Once a qualitative fit is obtained, the determined n and k are

stored as initial values, n_{1st} and k_{1st} , for the second step of fitting. In the second step, optimal values for n and k are found using a 300-step, hybrid Monte-Carlo Levenberg-Marquardt process to fit the data with n constrained to within 10% of n_{1st} of its starting value and k unconstrained. In the third step of fitting, the uncertainties in the optimal n_{2nd} , k_{2nd} values are assessed. For optimal fitting of the data in cases where the absorption coefficient is low ($k \approx 10^{-4}$), weights are added to the evaluation of the least squares values in the Monte-Carlo/Levenberg-Marquardt calculation, to give more weight to destructive interference and less weight to the constructive interference in the interferogram leads to a more accurate fit of the k values. The weights are defined as:

$$\text{weights} = \frac{|\text{interferogram} - \max(\text{interferogram})|}{\max |(\text{interferogram} - \max(\text{interferogram}))|} \quad (9)$$

Without weighting, the dips in the interferogram are not well represented, particularly when they are tens of decibels deep, resulting in large overestimates of the absorption coefficients.

In the fourth step, a two-dimensional grid of n , k values is used to generate a least-square 2D map, with n constrained to within 15% of its optimum value and k constrained to between 10^{-4} and 10^{-2} (corresponding to the dynamic range of the measurement setup). From this 2D map, a 95% confidence interval is extracted that is used to determine the uncertainties reported in **Table 1**. For frozen samples, ~ 5 interferograms are measured for 3 different sample thicknesses (generally 5.5, 11.4 and 18.2 mm). Frozen samples were far more challenging to fit than solid samples at room temperature. When possible, n and k are extracted from the best fits of the thickest samples and the error bar is extracted from those measurements.

Note that in some instances, the signal to noise ratio of the interferogram was too low to enable a fit and concomitant extraction of n and k . This is especially the case at high frequencies (*i.e.*, 920 GHz) where the sweep range is limited, and the absorption is large.

Custom MAS Rotors

Custom MAS rotors were fabricated using various ceramic materials [α -Al₂O₃ (sapphire), Y₂O₃:ZrO₂ (yttria-stabilized zirconia or YSZ), AlN (aluminum nitride), Si_{1-x}Al_xO_{1-x}N_x (β - SiALON)] machined by O'Keefe Ceramics (Woodland Park, CO). All of these materials are commonly used for rotors for ssNMR experiments [69,122,123]. Two commercially available rotors made from YSZ and α -Al₂O₃ were also characterized (Cortecnet, NY, USA). The custom-ordered rotors were machined with a sample space 0.5 mm deeper than that of a commercial standard-wall Bruker rotor (6% volume increase), which should not impact the DNP performance. Finally, values of n and k for these materials were obtained from slabs manufactured by O'Keefe Ceramics.

MAS-DNP experiments

MAS-DNP experiments were carried out on a 14.1 T spectrometer with a 395 GHz gyrotron μ w source. All DNP experiments (unless otherwise noted) were carried out using a ¹H-¹³C cross polarization (CP) sequence with a contact time of 1 ms, a ¹H radio-frequency (rf) amplitude ramp from 47 kHz to 52 kHz, and constant ¹³C rf amplitude at 42 kHz. During acquisition, the SPINAL64 decoupling sequence was used with a pulse power of 100 kHz [124]. Rotors were filled with 250 mM proline and 10 mM AMUPol (Cortecnet, NY, USA) dissolved in a 60% *d*₈-glycerol/30% D₂O/10% H₂O sample matrix. All samples were degassed by freeze-thaw cycling to ensure a buildup time, T_b , ranging between $\sim 4.8 - 5$ s [17,51]. For each rotor, the Martin-Puplett interferometer built into the μ w beam path was adjusted to maximize the DNP enhancement [40,70]. The μ w power at the sample was then optimized using the QO setup installed on the MAS-DNP instrument to reach the maximum enhancement value for each rotor [70]. It should be noted that the QO component of the MAS DNP instrument is not the same as the QO bench discussed in the previous section [70]. The MAS-DNP results are summarized in Table 2. The error bars were obtained by repeating the measurements multiple times. The error bar corresponds to the difference between the minimum and maximum enhancements obtained, $|\epsilon_{on/off}^{\max} - \epsilon_{on/off}^{\min}|$, and the measurements were carried out at least five times. The rotor caps for the custom rotors were machined by

RevolutionNMR. Due to the multiple rotor sizes, no soft plugs were used in the experiments.

Electromagnetic field simulations

The measured dielectric properties were used as inputs in CST Studio Suite electromagnetic field simulations to model the μW beam propagation in the sample space (Dassault Systèmes, Paris, France). Simulations assumed a 5 W Gaussian μW beam with a waist of 3.2 mm at 11 mm from the center of the rotor, corresponding to the geometry of our Bruker MAS-DNP probe and expected μW power at the end of the waveguide. Unless otherwise specified, the stator and coils were not included in simulations for simplicity.

To determine the μW nutation frequency, the \mathbf{H} field values for each voxel were projected into H_x , H_y , and H_z complex vectors [125]. Specifically, the \mathbf{H} field is first rotated so that the long axis of the rotor is at the magic angle with respect to the z axis that corresponds to the main magnetic field axis. The relevant portion of the field for nutation is the transverse vector, \mathbf{H}_{xy} , in the laboratory frame. This value corresponds to the averaged $\mathbf{H}_{xy}(t)$ over one irradiation period. For each voxel, \mathbf{H}_{xy} was projected and its norm, $\|H_{xy}\|$, was calculated. The average of all $\|H_{xy}\|$ across the rotor was then converted to the nutation frequency using $\nu_{1,e} = \gamma_e \|H_{xy}\| \mu_0 / 2\pi$, where γ_e is the gyromagnetic ratio of the radical electron and μ_0 is the permeability of free space.

MAS-DNP simulations – MAS-DNP simulations were run using the same model and parameters as described in ref [51]. The reader is referred to this reference for the details. For this article, we only replaced the nutation frequencies by the ones calculated using the simulation tool.

Acknowledgements

This work was performed at the National High Magnetic Field Laboratory, which is supported by National Science Foundation Agreement No. DMR-1644779, DMR-2128556 and the State of Florida. This

work was additionally funded by a postdoctoral scholar award from the Provost's Office at Florida State University, the National Institute of Health grant P41 GM122698 and RM1 GM148766 and the National Science Foundation, grant number CHEM-2203405 and CHE-1808660.

We thank Jonathan Marbey for helpful advice regarding the use of the VNA and sources. Additionally, we thank Dr. Sungsool Wi for the use of his laboratory space and Dr. William Brey for funding the workstation used for the CST simulations.

References

- [1] M. Rosay, L. Tometich, S. Pawsey, R. Bader, R. Schauwecker, M. Blank, P.M. Borchard, S.R. Cauffman, K.L. Felch, R.T. Weber, R.J. Temkin, R.G. Griffin, W.E. Maas, Solid-state dynamic nuclear polarization at 263 GHz: spectrometer design and experimental results, *Phys. Chem. Chem. Phys.* 12 (2010) 5850. <https://doi.org/10.1039/c003685b>.
- [2] M. Rosay, M. Blank, F. Engelke, Instrumentation for solid-state dynamic nuclear polarization with magic angle spinning NMR, *J. Magn. Reson.* 264 (2016) 88–98. <https://doi.org/10.1016/j.jmr.2015.12.026>.
- [3] M. Blank, K.L. Felch, Millimeter-Wave Sources for DNP-NMR, in: *eMagRes*, John Wiley & Sons, Ltd, 2018: pp. 155–166. <https://doi.org/10.1002/9780470034590.emrstm1582>.
- [4] Y. Matsuki, T. Kobayashi, J. Fukazawa, F.A. Perras, M. Pruski, T. Fujiwara, Efficiency analysis of helium-cooled MAS DNP: case studies of surface-modified nanoparticles and homogeneous small-molecule solutions, *Phys. Chem. Chem. Phys.* 23 (2021) 4919–4926. <https://doi.org/10.1039/D0CP05658H>.
- [5] A.J. Rossini, A. Zagdoun, M. Lelli, A. Lesage, C. Copéret, L. Emsley, Dynamic Nuclear Polarization Surface Enhanced NMR Spectroscopy, *Acc. Chem. Res.* 46 (2013) 1942–1951. <https://doi.org/10.1021/ar300322x>.

- [6] Q.Z. Ni, E. Daviso, T.V. Can, E. Markhasin, S.K. Jawla, T.M. Swager, R.J. Temkin, J. Herzfeld, R.G. Griffin, High Frequency Dynamic Nuclear Polarization, *Acc. Chem. Res.* 46 (2013) 1933–1941. <https://doi.org/10.1021/ar300348n>.
- [7] T. Jacso, W.T. Franks, H. Rose, U. Fink, J. Broecker, S. Keller, H. Oschkinat, B. Reif, Characterization of Membrane Proteins in Isolated Native Cellular Membranes by Dynamic Nuclear Polarization Solid-State NMR Spectroscopy without Purification and Reconstitution, *Angew. Chem. Int. Ed.* 51 (2012) 432–435. <https://doi.org/10.1002/anie.201104987>.
- [8] W.Y. Chow, B.P. Norman, N.B. Roberts, L.R. Ranganath, C. Teutloff, R. Bittl, M.J. Duer, J.A. Gallagher, H. Oschkinat, Pigmentation Chemistry and Radical-Based Collagen Degradation in Alkaptonuria and Osteoarthritic Cartilage, *Angew. Chem. Int. Ed.* 59 (2020) 11937–11942. <https://doi.org/10.1002/anie.202000618>.
- [9] B.J. Albert, C. Gao, E.L. Sesti, E.P. Saliba, N. Alaniva, F.J. Scott, S.Th. Sigurdsson, A.B. Barnes, Dynamic Nuclear Polarization Nuclear Magnetic Resonance in Human Cells Using Fluorescent Polarizing Agents, *Biochemistry* 57 (2018) 4741–4746. <https://doi.org/10.1021/acs.biochem.8b00257>.
- [10] A.L. Paioni, M.A.M. Renault, M. Baldus, DNP and Cellular Solid-State NMR, in: *eMagRes*, John Wiley & Sons, Ltd, 2018: pp. 51–62. <https://doi.org/10.1002/9780470034590.emrstm1561>.
- [11] D. Lee, S. Hediger, G. De Paëpe, Is solid-state NMR enhanced by dynamic nuclear polarization?, *Solid State Nucl. Magn. Reson.* 66–67 (2015) 6–20. <https://doi.org/10.1016/j.ssnmr.2015.01.003>.
- [12] A. Lesage, M. Lelli, D. Gajan, M.A. Caporini, V. Vitzthum, P. Miéville, J. Alauzun, A. Roussey, C. Thieuleux, A. Mehdi, G. Bodenhausen, C. Coperet, L. Emsley, Surface Enhanced NMR Spectroscopy by Dynamic Nuclear Polarization, *J. Am. Chem. Soc.* 132 (2010) 15459–15461. <https://doi.org/10.1021/ja104771z>.
- [13] H. Takahashi, S. Hediger, G. De Paëpe, Matrix-free dynamic nuclear polarization enables solid-state NMR ^{13}C – ^{13}C correlation spectroscopy of proteins at natural isotopic abundance, *Chem. Commun.* 49 (2013) 9479. <https://doi.org/10.1039/c3cc45195j>.
- [14] X. Kang, A. Kirui, A. Muszyński, M.C.D. Widanage, A. Chen, P. Azadi, P. Wang, F. Mentink-Vigier, T. Wang, Molecular architecture of fungal cell walls revealed by solid-state NMR, *Nat. Commun.* 9 (2018) 2747. <https://doi.org/10.1038/s41467-018-05199-0>.
- [15] A.G.M. Rankin, J. Trébosc, F. Pourpoint, J.-P. Amoureux, O. Lafon, Recent developments in MAS DNP-NMR of materials, *Solid State Nucl. Magn. Reson.* 101 (2019) 116–143. <https://doi.org/10.1016/j.ssnmr.2019.05.009>.
- [16] P.C.A. van der Wel, K.-N. Hu, J. Lewandowski, R.G. Griffin, Dynamic Nuclear Polarization of Amyloidogenic Peptide Nanocrystals: GNNQQNY, a Core Segment of the Yeast Prion Protein Sup35p, *J. Am. Chem. Soc.* 128 (2006) 10840–10846. <https://doi.org/10.1021/ja0626685>.
- [17] C. Sauvée, M. Rosay, G. Casano, F. Aussenac, R.T. Weber, O. Ouari, P. Tordo, Highly Efficient, Water-Soluble Polarizing Agents for Dynamic Nuclear Polarization at High Frequency, *Angew. Chem. Int. Ed.* 52 (2013) 10858–10861. <https://doi.org/10.1002/anie.201304657>.
- [18] A. Zagdoun, G. Casano, O. Ouari, G. Lapadula, A.J. Rossini, M. Lelli, M. Baffert, D. Gajan, L. Veyre, W.E. Maas, M. Rosay, R.T. Weber, C. Thieuleux, C. Coperet, A. Lesage, P. Tordo, L. Emsley, A Slowly Relaxing Rigid Biradical for Efficient Dynamic Nuclear Polarization Surface-Enhanced NMR Spectroscopy: Expedient Characterization of Functional Group Manipulation in Hybrid Materials, *J. Am. Chem. Soc.* 134 (2012) 2284–2291. <https://doi.org/10.1021/ja210177v>.

- [19] G. Mathies, M.A. Caporini, V.K. Michaelis, Y. Liu, K.-N. Hu, D. Mance, J.L. Zweier, M. Rosay, M. Baldus, R.G. Griffin, Efficient Dynamic Nuclear Polarization at 800 MHz/527 GHz with Trityl-Nitroxide Biradicals, *Angew. Chem.* 127 (2015) 11936–11940. <https://doi.org/10.1002/ange.201504292>.
- [20] A.P. Jagtap, M.-A. Geiger, D. Stöppler, M. Orwick-Rydmark, H. Oschkinat, S.Th. Sigurdsson, bcTol: a highly water-soluble biradical for efficient dynamic nuclear polarization of biomolecules, *Chem. Commun.* 52 (2016) 7020–7023. <https://doi.org/10.1039/C6CC01813K>.
- [21] A. Lund, G. Casano, G. Menzildjian, M. Kaushik, G. Stevanato, M. Yulikov, R. Jabbour, D. Wisser, M. Renom-Carrasco, C. Thieuleux, F. Bernada, H. Karoui, D. Siri, M. Rosay, I.V. Sergeev, D. Gajan, M. Lelli, L. Emsley, O. Ouari, A. Lesage, TinyPols: a family of water-soluble binitroxides tailored for dynamic nuclear polarization enhanced NMR spectroscopy at 18.8 and 21.1 T, *Chem. Sci.* 11 (2020) 2810–2818. <https://doi.org/10.1039/C9SC05384K>.
- [22] F. Mentink-Vigier, I. Marin-Montesinos, A.P. Jagtap, T. Halbritter, J. van Tol, S. Hediger, D. Lee, S.Th. Sigurdsson, G. De Paëpe, Computationally Assisted Design of Polarizing Agents for Dynamic Nuclear Polarization Enhanced NMR: The AsymPol Family, *J. Am. Chem. Soc.* 140 (2018) 11013–11019. <https://doi.org/10.1021/jacs.8b04911>.
- [23] R. Harrabi, T. Halbritter, F. Aussenac, O. Dakhlaoui, J. van Tol, K.K. Damodaran, D. Lee, S. Paul, S. Hediger, F. Mentink-Vigier, S.Th. Sigurdsson, G. De Paëpe, Highly Efficient Polarizing Agents for MAS-DNP of Proton-Dense Molecular Solids, *Angew. Chem. Int. Ed.* 61 (2022) e202114103. <https://doi.org/10.1002/anie.202114103>.
- [24] T. Halbritter, R. Harrabi, S. Paul, J. Van Tol, D. Lee, S. Hediger, S.Th. Sigurdsson, F. Mentink-Vigier, G. De Paëpe, PyrroTriPol: a semi-rigid trityl-nitroxide for high field dynamic nuclear polarization, *Chem. Sci.* 14 (2023) 3852–3864. <https://doi.org/10.1039/D2SC05880D>.
- [25] D. Wisser, G. Karthikeyan, A. Lund, G. Casano, H. Karoui, M. Yulikov, G. Menzildjian, A.C. Pinon, A. Pureau, F. Engelke, S.R. Chaudhari, D. Kubicki, A.J. Rossini, I.B. Moroz, D. Gajan, C. Copéret, G. Jeschke, M. Lelli, L. Emsley, A. Lesage, O. Ouari, BDPA-Nitroxide Biradicals Tailored for Efficient Dynamic Nuclear Polarization Enhanced Solid-State NMR at Magnetic Fields up to 21.1 T, *J. Am. Chem. Soc.* 140 (2018) 13340–13349. <https://doi.org/10.1021/jacs.8b08081>.
- [26] C. Sauvée, G. Casano, S. Abel, A. Rockenbauer, D. Akhmetzyanov, H. Karoui, D. Siri, F. Aussenac, W. Maas, R.T. Weber, T. Prisner, M. Rosay, P. Tordo, O. Ouari, Tailoring of Polarizing Agents in the bTurea Series for Cross-Effect Dynamic Nuclear Polarization in Aqueous Media, *Chem. - Eur. J.* 22 (2016) 5598–5606. <https://doi.org/10.1002/chem.201504693>.
- [27] D.J. Kubicki, G. Casano, M. Schwarzwälder, S. Abel, C. Sauvée, K. Ganesan, M. Yulikov, A.J. Rossini, G. Jeschke, C. Copéret, A. Lesage, P. Tordo, O. Ouari, L. Emsley, Rational design of dinitroxide biradicals for efficient cross-effect dynamic nuclear polarization, *Chem. Sci.* 7 (2015) 550–558. <https://doi.org/10.1039/C5SC02921J>.
- [28] F.A. Perras, R.R. Reinig, I.I. Slowing, A.D. Sadow, M. Pruski, Effects of biradical deuteration on the performance of DNP: towards better performing polarizing agents, *Phys. Chem. Chem. Phys.* 18 (2016) 65–69. <https://doi.org/10.1039/C5CP06505D>.
- [29] T.V. Can, M.A. Caporini, F. Mentink-Vigier, B. Corzilius, J.J. Walsh, M. Rosay, W.E. Maas, M. Baldus, S. Vega, T.M. Swager, R.G. Griffin, Overhauser effects in insulating solids, *J. Chem. Phys.* 141 (2014) 064202. <https://doi.org/10.1063/1.4891866>.
- [30] A. Gurinov, B. Sieland, A. Kuzhelev, H. Elgabarty, T.D. Kühne, T. Prisner, J. Paradies, M. Baldus, K.L. Ivanov, S. Pylaeva, Mixed-Valence Compounds as Polarizing Agents for Overhauser Dynamic Nuclear Polarization in Solids**, *Angew. Chem. Int. Ed.*

- 60 (2021) 15371–15375.
<https://doi.org/10.1002/anie.202103215>.
- [31] F.A. Perras, D.F. Flesariu, S.A. Southern, C. Nicolaidis, J.D. Bazak, N.M. Washton, T. Trypiniotis, C.P. Constantinides, P.A. Koutentis, Methyl-Driven Overhauser Dynamic Nuclear Polarization, *J. Phys. Chem. Lett.* 13 (2022) 4000–4006.
<https://doi.org/10.1021/acs.jpcclett.2c00748>.
- [32] W. Zhai, A. Lucini Paioni, X. Cai, S. Narasimhan, J. Medeiros-Silva, W. Zhang, A. Rockenbauer, M. Weingarth, Y. Song, M. Baldus, Y. Liu, Postmodification via Thiol-Click Chemistry Yields Hydrophilic Trityl-Nitroxide Biradicals for Biomolecular High-Field Dynamic Nuclear Polarization, *J. Phys. Chem. B* 124 (2020) 9047–9060. <https://doi.org/10.1021/acs.jpcc.0c08321>.
- [33] R. Yao, D. Beriashvili, W. Zhang, S. Li, A. Safeer, A. Gurinov, A. Rockenbauer, Y. Yang, Y. Song, M. Baldus, Y. Liu, Highly bioresistant, hydrophilic and rigidly linked trityl-nitroxide biradicals for cellular high-field dynamic nuclear polarization, *Chem. Sci.* 13 (2022) 14157–14164.
<https://doi.org/10.1039/D2SC04668G>.
- [34] R. Rogawski, I.V. Sergeyev, Y. Li, M.F. Ottaviani, V. Cornish, A.E. McDermott, Dynamic Nuclear Polarization Signal Enhancement with High-Affinity Biradical Tags, *J. Phys. Chem. B* 121 (2017) 1169–1175.
<https://doi.org/10.1021/acs.jpcc.6b09021>.
- [35] M.-A. Geiger, M. Orwick-Rydmark, K. Märker, W.T. Franks, D. Akhmetzyanov, D. Stöppler, M. Zinke, E. Specker, M. Nazaré, A. Diehl, B.-J. van Rossum, F. Aussenac, T. Prisner, Ü. Akbey, H. Oschkinat, Temperature dependence of cross-effect dynamic nuclear polarization in rotating solids: advantages of elevated temperatures, *Phys. Chem. Chem. Phys.* 18 (2016) 30696–30704. <https://doi.org/10.1039/C6CP06154K>.
- [36] E. Ravera, B. Corzilius, V.K. Michaelis, C. Luchinat, R.G. Griffin, I. Bertini, DNP-Enhanced MAS NMR of Bovine Serum Albumin Sediments and Solutions, *J. Phys. Chem. B* 118 (2014) 2957–2965.
<https://doi.org/10.1021/jp500016f>.
- [37] D. Gajan, M. Schwarzwälder, M.P. Conley, W.R. Grüning, A.J. Rossini, A. Zagdoun, M. Lelli, M. Yulikov, G. Jeschke, C. Sauvée, O. Ouari, P. Tordo, L. Veyre, A. Lesage, C. Thieuleux, L. Emsley, C. Copéret, Solid-Phase Polarization Matrixes for Dynamic Nuclear Polarization from Homogeneously Distributed Radicals in Mesostructured Hybrid Silica Materials, *J. Am. Chem. Soc.* 135 (2013) 15459–15466.
<https://doi.org/10.1021/ja405822h>.
- [38] A.N. Smith, M.A. Caporini, G.E. Fanucci, J.R. Long, A Method for Dynamic Nuclear Polarization Enhancement of Membrane Proteins, *Angew. Chem. Int. Ed.* 54 (2015) 1542–1546.
<https://doi.org/10.1002/anie.201410249>.
- [39] Y. Matsuki, K. Ueda, T. Idehara, R. Ikeda, I. Ogawa, S. Nakamura, M. Toda, T. Anai, T. Fujiwara, Helium-cooling and -spinning dynamic nuclear polarization for sensitivity-enhanced solid-state NMR at 14T and 30K, *J. Magn. Reson.* 225 (2012) 1–9.
<https://doi.org/10.1016/j.jmr.2012.09.008>.
- [40] K.R. Thurber, A. Potapov, W.-M. Yau, R. Tycko, Solid state nuclear magnetic resonance with magic-angle spinning and dynamic nuclear polarization below 25K, *J. Magn. Reson.* 226 (2013) 100–106.
<https://doi.org/10.1016/j.jmr.2012.11.009>.
- [41] E. Bouleau, P. Saint-Bonnet, F. Mentink-Vigier, H. Takahashi, J.-F. Jacquot, M. Bardet, F. Aussenac, A. Pureau, F. Engelke, S. Hediger, D. Lee, G. De Paëpe, Pushing NMR sensitivity limits using dynamic nuclear polarization with closed-loop cryogenic helium sample spinning, *Chem. Sci.* 6 (2015) 6806–6812.
<https://doi.org/10.1039/C5SC02819A>.
- [42] E. Bouleau, D. Lee, P. Saint-Bonnet, S. Hediger, G. De Paëpe, Ultra-Low Temperature Nuclear Magnetic Resonance, *IOP Conf. Ser. Mater. Sci. Eng.* 171 (2017) 012142.
<https://doi.org/10.1088/1757-899X/171/1/012142>.

- [43] K. Thurber, R. Tycko, Low-temperature dynamic nuclear polarization with helium-cooled samples and nitrogen-driven magic-angle spinning, *J. Magn. Reson.* 264 (2016) 99–106. <https://doi.org/10.1016/j.jmr.2016.01.011>.
- [44] Y. Matsuki, T. Fujiwara, Advances in High-Field DNP Methods, in: *The Nuclear Magnetic Resonance Soci (Ed.), Exp. Approaches NMR Spectrosc.*, Springer Singapore, Singapore, 2018: pp. 91–134. https://doi.org/10.1007/978-981-10-5966-7_4.
- [45] Y. Matsuki, T. Fujiwara, Cryogenic Platforms and Optimized DNP Sensitivity, in: *eMagRes*, John Wiley & Sons, Ltd, 2018: pp. 9–24. <https://doi.org/10.1002/9780470034590.emrstm1553>.
- [46] S. Paul, E. Bouleau, Q. Reynard-Feytis, J.-P. Arnaud, F. Bancel, B. Rollet, P. Dalban-Moreynas, C. Reiter, A. Porea, F. Engelke, S. Hediger, G. De Paëpe, Sustainable and cost-effective MAS DNP-NMR at 30 K with cryogenic sample exchange, *J. Magn. Reson.* 356 (2023) 107561. <https://doi.org/10.1016/j.jmr.2023.107561>.
- [47] F.J. Scott, E.P. Saliba, B.J. Albert, N. Alaniva, E.L. Sesti, C. Gao, N.C. Golota, E.J. Choi, A.P. Jagtap, J.J. Wittmann, M. Eckardt, W. Harneit, B. Corzilius, S. Th. Sigurdsson, A.B. Barnes, Frequency-agile gyrotron for electron decoupling and pulsed dynamic nuclear polarization, *J. Magn. Reson.* 289 (2018) 45–54. <https://doi.org/10.1016/j.jmr.2018.02.010>.
- [48] A. Porea, C. Reiter, A.I. Dimitriadis, E. de Rijk, F. Aussenac, I. Sergeev, M. Rosay, F. Engelke, Improved waveguide coupling for 1.3 mm MAS DNP probes at 263 GHz, *J. Magn. Reson.* 302 (2019) 43–49. <https://doi.org/10.1016/j.jmr.2019.03.009>.
- [49] T.A. Siaw, A. Leavesley, A. Lund, I. Kaminker, S. Han, A versatile and modular quasi optics-based 200 GHz dual dynamic nuclear polarization and electron paramagnetic resonance instrument, *J. Magn. Reson.* 264 (2016) 131–153. <https://doi.org/10.1016/j.jmr.2015.12.012>.
- [50] F. Mentink-Vigier, A.-L. Barra, J. van Tol, S. Hediger, D. Lee, G. De Paëpe, *De novo* prediction of cross-effect efficiency for magic angle spinning dynamic nuclear polarization, *Phys. Chem. Chem. Phys.* 21 (2019) 2166–2176. <https://doi.org/10.1039/C8CP06819D>.
- [51] F. Mentink-Vigier, T. Dubroca, J. Van Tol, S.Th. Sigurdsson, The distance between g-tensors of nitroxide biradicals governs MAS-DNP performance: The case of the bTurea family, *J. Magn. Reson.* 329 (2021) 107026. <https://doi.org/10.1016/j.jmr.2021.107026>.
- [52] L.R. Becerra, G.J. Gerfen, R.J. Temkin, D.J. Singel, R.G. Griffin, Dynamic nuclear polarization with a cyclotron resonance maser at 5 T, *Phys. Rev. Lett.* 71 (1993) 3561–3564. <https://doi.org/10.1103/PhysRevLett.71.3561>.
- [53] S. Björgvinsdóttir, B.J. Walder, A.C. Pinon, J.R. Yarava, L. Emsley, DNP enhanced NMR with flip-back recovery, *J. Magn. Reson.* 288 (2018) 69–75. <https://doi.org/10.1016/j.jmr.2018.01.017>.
- [54] D. Mance, P. Gast, M. Huber, M. Baldus, K.L. Ivanov, The magnetic field dependence of cross-effect dynamic nuclear polarization under magic angle spinning, *J. Chem. Phys.* 142 (2015) 234201. <https://doi.org/10.1063/1.4922219>.
- [55] F. Mentink-Vigier, S. Paul, D. Lee, A. Feintuch, S. Hediger, S. Vega, G. De Paëpe, Nuclear depolarization and absolute sensitivity in magic-angle spinning cross effect dynamic nuclear polarization, *Phys. Chem. Chem. Phys.* 17 (2015) 21824–21836. <https://doi.org/10.1039/C5CP03457D>.
- [56] K.R. Thurber, R. Tycko, Perturbation of nuclear spin polarizations in solid state NMR of nitroxide-doped samples by magic-angle spinning without microwaves., *J. Chem. Phys.* 140 (2014) 184201. <https://doi.org/10.1063/1.4874341>.
- [57] F. Mentink-Vigier, S. Vega, G. De Paëpe, Fast and accurate MAS-DNP simulations of large spin ensembles, *Phys. Chem. Chem. Phys.* 19

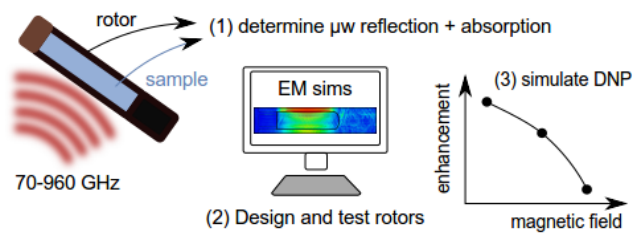
- (2017) 3506–3522. <https://doi.org/10.1039/C6CP07881H>.
- [58] F. Mentink-Vigier, Ü. Akbey, H. Oschkinat, S. Vega, A. Feintuch, Theoretical aspects of Magic Angle Spinning - Dynamic Nuclear Polarization, *J. Magn. Reson.* 258 (2015) 102–120. <https://doi.org/10.1016/j.jmr.2015.07.001>.
- [59] K.R. Thurber, R. Tycko, Theory for cross effect dynamic nuclear polarization under magic-angle spinning in solid state nuclear magnetic resonance: The importance of level crossings, *J. Chem. Phys.* 137 (2012) 084508. <https://doi.org/10.1063/1.4747449>.
- [60] F. Mentink-Vigier, Ü. Akbey, Y. Hovav, S. Vega, H. Oschkinat, A. Feintuch, Fast passage dynamic nuclear polarization on rotating solids, *J. Magn. Reson.* 224 (2012) 13–21. <https://doi.org/10.1016/j.jmr.2012.08.013>.
- [61] A. Equbal, K. Tagami, S. Han, Pulse-Shaped Dynamic Nuclear Polarization under Magic-Angle Spinning, *J. Phys. Chem. Lett.* 10 (2019) 7781–7788. <https://doi.org/10.1021/acs.jpcclett.9b03070>.
- [62] F. Mentink-Vigier, G. Mathies, Y. Liu, A.-L. Barra, M.A. Caporini, D. Lee, S. Hediger, R. G. Griffin, G. De Paëpe, Efficient cross-effect dynamic nuclear polarization without depolarization in high-resolution MAS NMR, *Chem. Sci.* 8 (2017) 8150–8163. <https://doi.org/10.1039/C7SC02199B>.
- [63] S.R. Chaudhari, P. Berruyer, D. Gajan, C. Reiter, F. Engelke, D.L. Silverio, C. Copéret, M. Lelli, A. Lesage, L. Emsley, Dynamic nuclear polarization at 40 kHz magic angle spinning, *Phys. Chem. Chem. Phys.* 18 (2016) 10616–10622. <https://doi.org/10.1039/C6CP00839A>.
- [64] D.J. Kubicki, A.J. Rossini, A. Porea, A. Zagdoun, O. Ouari, P. Tordo, F. Engelke, A. Lesage, L. Emsley, Amplifying Dynamic Nuclear Polarization of Frozen Solutions by Incorporating Dielectric Particles, *J. Am. Chem. Soc.* 136 (2014) 15711–15718. <https://doi.org/10.1021/ja5088453>.
- [65] F.A. Perras, T. Kobayashi, M. Pruski, Magnetic resonance imaging of DNP enhancements in a rotor spinning at the magic angle, *J. Magn. Reson.* 264 (2016) 125–130. <https://doi.org/10.1016/j.jmr.2016.01.004>.
- [66] E.A. Nanni, A.B. Barnes, Y. Matsuki, P.P. Woskov, B. Corzilius, R.G. Griffin, R.J. Temkin, Microwave field distribution in a magic angle spinning dynamic nuclear polarization NMR probe, *J. Magn. Reson.* 210 (2011) 16–23. <https://doi.org/10.1016/j.jmr.2011.02.001>.
- [67] D.E.M. Hoff, B.J. Albert, E.P. Saliba, F.J. Scott, E.J. Choi, M. Mardini, A.B. Barnes, Frequency swept microwaves for hyperfine decoupling and time domain dynamic nuclear polarization, *Solid State Nucl. Magn. Reson.* 72 (2015) 79–89.
- [68] M.P. Hanrahan, Y. Chen, R. Blome-Fernández, J.L. Stein, G.F. Pach, M.A.S. Adamson, N.R. Neale, B.M. Cossairt, J. Vela, A.J. Rossini, Probing the Surface Structure of Semiconductor Nanoparticles by DNP SENS with Dielectric Support Materials, *J. Am. Chem. Soc.* 141 (2019) 15532–15546. <https://doi.org/10.1021/jacs.9b05509>.
- [69] K.J. Pike, T.F. Kemp, H. Takahashi, R. Day, A.P. Howes, E.V. Kryukov, J.F. MacDonald, A.E.C. Collis, D.R. Bolton, R.J. Wylde, M. Orwick, K. Kosuga, A.J. Clark, T. Idehara, A. Watts, G.M. Smith, M.E. Newton, R. Dupree, M.E. Smith, A spectrometer designed for 6.7 and 14.1T DNP-enhanced solid-state MAS NMR using quasi-optical microwave transmission, *J. Magn. Reson.* 215 (2012) 1–9. <https://doi.org/10.1016/j.jmr.2011.12.006>.
- [70] T. Dubroca, A.N. Smith, K.J. Pike, S. Froud, R. Wylde, B. Trociewitz, J. McKay, F. Mentink-Vigier, J. van Tol, S. Wi, W. Brey, J.R. Long, L. Frydman, S. Hill, A quasi-optical and corrugated waveguide microwave transmission system for simultaneous dynamic nuclear polarization NMR on two separate 14.1 T spectrometers, *J. Magn. Reson.* 289 (2018) 35–44. <https://doi.org/10.1016/j.jmr.2018.01.015>.
- [71] M. Rosay, I. Scrgyev, L. Tometich, C. Hickey, A. Roitman, D. Yake, D. Berry, Opportunities

- and Challenges for EIK's in DNP NMR Applications, in: 2018 43rd Int. Conf. Infrared Millim. Terahertz Waves IRMMW-THz, IEEE, Nagoya, 2018: pp. 1–2. <https://doi.org/10.1109/IRMMW-THz.2018.8510328>.
- [72] I.V. Sergeev, F. Aussenac, A. Porea, C. Reiter, E. Bryerton, S. Retzloff, J. Hesler, L. Tometich, M. Rosay, Efficient 263 GHz magic angle spinning DNP at 100 K using solid-state diode sources, *Solid State Nucl. Magn. Reson.* 100 (2019) 63–69. <https://doi.org/10.1016/j.ssnmr.2019.03.008>.
- [73] M.L. Mesenbrink, Complex indices of refraction for water and ice from visible to long wavelengths, Florida State University, 1996.
- [74] J. Mcentee, The terahertz gap: into the dead zone, *Chem. World* (n.d.). <https://www.chemistryworld.com/features/the-terahertz-gap-into-the-dead-zone/3004857.article> (accessed March 14, 2024).
- [75] A. Henstra, P. Dirksen, J. Schmidt, W.T. Wenckebach, Nuclear spin orientation via electron spin locking (NOVEL), *J. Magn. Reson.* 1969 77 (1988) 389–393. [https://doi.org/10.1016/0022-2364\(88\)90190-4](https://doi.org/10.1016/0022-2364(88)90190-4).
- [76] T.V. Can, R.T. Weber, J.J. Walish, T.M. Swager, R.G. Griffin, Frequency-Swept Integrated Solid Effect, *Angew. Chem. Int. Ed.* 56 (2017) 6744–6748. <https://doi.org/10.1002/anie.201700032>.
- [77] T.V. Can, R.T. Weber, J.J. Walish, T.M. Swager, R.G. Griffin, Ramped-amplitude NOVEL, *J. Chem. Phys.* 146 (2017) 154204. <https://doi.org/10.1063/1.4980155>.
- [78] K.O. Tan, C. Yang, R.T. Weber, G. Mathies, R.G. Griffin, Time-optimized pulsed dynamic nuclear polarization, *Sci. Adv.* 5 (2019) eaav6909. <https://doi.org/10.1126/sciadv.aav6909>.
- [79] G. Mathies, S. Jain, M. Reese, R.G. Griffin, Pulsed Dynamic Nuclear Polarization with Trityl Radicals, *J. Phys. Chem. Lett.* 7 (2016) 111–116. <https://doi.org/10.1021/acs.jpcclett.5b02720>.
- [80] S.K. Jain, G. Mathies, R.G. Griffin, Off-resonance NOVEL, *J. Chem. Phys.* 147 (2017) 164201. <https://doi.org/10.1063/1.5000528>.
- [81] V.S. Redrouthu, G. Mathies, Efficient Pulsed Dynamic Nuclear Polarization with the X-Inverse-X Sequence, *J. Am. Chem. Soc.* 144 (2022) 1513–1516. <https://doi.org/10.1021/jacs.1c09900>.
- [82] T.V. Can, J.E. McKay, R.T. Weber, C. Yang, T. Dubroca, J. van Tol, S. Hill, R.G. Griffin, Frequency-Swept Integrated and Stretched Solid Effect Dynamic Nuclear Polarization, *J. Phys. Chem. Lett.* 9 (2018) 3187–3192. <https://doi.org/10.1021/acs.jpcclett.8b01002>.
- [83] Y. Quan, M.V.H. Subramanya, Y. Ouyang, M. Mardini, T. Dubroca, S. Hill, R.G. Griffin, Coherent Dynamic Nuclear Polarization using Chirped Pulses, *J. Phys. Chem. Lett.* 14 (2023) 4748–4753. <https://doi.org/10.1021/acs.jpcclett.3c00726>.
- [84] D.A. Hall, D.C. Maus, G.J. Gerfen, S.J. Inati, L.R. Becerra, F.W. Dahlquist, R.G. Griffin, Polarization-Enhanced NMR Spectroscopy of Biomolecules in Frozen Solution, *Science* 276 (1997) 930–932. <https://doi.org/10.1126/science.276.5314.930>.
- [85] A. Zagdoun, A.J. Rossini, D. Gajan, A. Bourdolle, O. Ouari, M. Rosay, W.E. Maas, P. Tordo, M. Lelli, L. Emsley, A. Lesage, C. Copéret, Non-aqueous solvents for DNP surface enhanced NMR spectroscopy, *Chem Commun* 48 (2012) 654–656. <https://doi.org/10.1039/C1CC15242D>.
- [86] S.G. Warren, R.E. Brandt, Optical constants of ice from the ultraviolet to the microwave: A revised compilation, *J. Geophys. Res.* 113 (2008) D14220. <https://doi.org/10.1029/2007JD009744>.
- [87] P.F. Goldsmith, Quasioptical systems: Gaussian beam quasioptical propagation and applications, IEEE Press, Piscataway, NJ, 1998.

- [88] R.G. LeBel, D.A.I. Goring, Density, Viscosity, Refractive Index, and Hygroscopicity of Mixtures of Water and Dimethyl Sulfoxide., *J. Chem. Eng. Data* 7 (1962) 100–101. <https://doi.org/10.1021/jc60012a032>.
- [89] C.L. Motion, S.L. Cassidy, P.A.S. Cruickshank, R.I. Hunter, D.R. Bolton, H. El Mkami, S. Van Doorslaer, J.E. Lovett, G.M. Smith, The use of composite pulses for improving DEER signal at 94 GHz, *J. Magn. Reson.* 278 (2017) 122–133. <https://doi.org/10.1016/j.jmr.2017.03.018>.
- [90] M.L. Mak-Jurkauskas, V.S. Bajaj, M.K. Hornstein, M. Belenky, R.G. Griffin, J. Herzfeld, Energy transformations early in the bacteriorhodopsin photocycle revealed by DNP-enhanced solid-state NMR, *Proc. Natl. Acad. Sci.* 105 (2008) 883–888. <https://doi.org/10.1073/pnas.0706156105>.
- [91] J.E. Kent, B.E. Ackermann, G.T. Debelouchina, F.M. Marassi, Dynamic Nuclear Polarization Illuminates Key Protein–Lipid Interactions in the Native Bacterial Cell Envelope, *Biochemistry* (2023). <https://doi.org/10.1021/acs.biochem.3c00262>.
- [92] A.N. Smith, U.T. Twahir, T. Dubroca, G.E. Fanucci, J.R. Long, Molecular Rationale for Improved Dynamic Nuclear Polarization of Biomembranes, *J. Phys. Chem. B* 120 (2016) 7880–7888. <https://doi.org/10.1021/acs.jpcc.6b02885>.
- [93] M.R. Elkins, I.V. Sergeyev, M. Hong, Determining Cholesterol Binding to Membrane Proteins by Cholesterol ¹³ C Labeling in Yeast and Dynamic Nuclear Polarization NMR, *J. Am. Chem. Soc.* 140 (2018) 15437–15449. <https://doi.org/10.1021/jacs.8b09658>.
- [94] R. Gupta, M. Lu, G. Hou, M.A. Caporini, M. Rosay, W. Maas, J. Struppe, C. Suiter, J. Ahn, I.-J.L. Byeon, W.T. Franks, M. Orwick-Rydmark, A. Bertarello, H. Oschkinat, A. Lesage, G. Pintacuda, A.M. Gronenborn, T. Polenova, Dynamic Nuclear Polarization Enhanced MAS NMR Spectroscopy for Structural Analysis of HIV-1 Protein Assemblies, *J. Phys. Chem. B* 120 (2016) 329–339. <https://doi.org/10.1021/acs.jpcc.5b12134>.
- [95] D. Gauto, O. Dakhlaoui, I. Marin-Montesinos, S. Hediger, G. De Paëpe, Targeted DNP for biomolecular solid-state NMR, *Chem. Sci.* 12 (2021) 6223–6237. <https://doi.org/10.1039/D0SC06959K>.
- [96] S. Bahri, R. Silvers, B. Michael, K. Jaudzems, D. Lalli, G. Casano, O. Ouari, A. Lesage, G. Pintacuda, S. Linse, R.G. Griffin, ¹H detection and dynamic nuclear polarization-enhanced NMR of A β ₁₋₄₂ fibrils, *Proc. Natl. Acad. Sci.* 119 (2022) e2114413119. <https://doi.org/10.1073/pnas.2114413119>.
- [97] K. Jaudzems, A. Bertarello, S.R. Chaudhari, A. Pica, D. Cala-De Paepe, E. Barbet-Massin, A.J. Pell, I. Akopjana, S. Kotelovica, D. Gajan, O. Ouari, K. Tars, G. Pintacuda, A. Lesage, Dynamic Nuclear Polarization-Enhanced Biomolecular NMR Spectroscopy at High Magnetic Field with Fast Magic-Angle Spinning, *Angew. Chem. Int. Ed.* 57 (2018) 7458–7462. <https://doi.org/10.1002/anie.201801016>.
- [98] G. Daian, A. Taube, A. Birnboim, Y. Shramkov, M. Daian, Measuring the dielectric properties of wood at microwave frequencies, *Wood Sci. Technol.* 39 (2005) 215–223. <https://doi.org/10.1007/s00226-004-0281-1>.
- [99] V.I. Suslyaev, T.D. Kochetkova, G.E. Dunaevskii, K.V. Dorozhkin, Research of dielectric properties of wood at frequencies 0.1 ÷ 0.5 THz, in: 2014 39th Int. Conf. Infrared Millim. Terahertz Waves IRMMW-THz, IEEE, Tucson, AZ, USA, 2014: pp. 1–2. <https://doi.org/10.1109/IRMMW-THz.2014.6956102>.
- [100] K. Zhou, S. Caroopen, Y. Delorme, M. Batrung, M. Gheudin, S. Shi, Dielectric Constant and Loss Tangent of Silicon at 700–900 GHz at Cryogenic Temperatures, *IEEE Microw. Wirel. Compon. Lett.* 29 (2019) 501–503. <https://doi.org/10.1109/LMWC.2019.2920532>.

- [101] G. Li, B. Dastrup, R.S. Palani, M.A. Shapiro, S.K. Jawla, R.G. Griffin, K.A. Nelson, R.J. Temkin, Design and optimization of THz coupling in zirconia MAS rotors for dynamic nuclear polarization NMR, *J. Magn. Reson.* (2024) 107722. <https://doi.org/10.1016/j.jmr.2024.107722>.
- [102] M.N. Afsar, I.I. Tkachov, K.N. Kocharyan, A novel W-band spectrometer for dielectric measurements, in: 2000 IEEE MTT- Int. Microw. Symp. Dig. Cat No00CH37017, IEEE, Boston, MA, USA, 2000: pp. 1627–1630. <https://doi.org/10.1109/MWSYM.2000.862289>.
- [103] R.I. Hunter, D.A. Robertson, J.C.G. Lesurf, INTERCOMPARISON OF QUASI-OPTICAL AND WAVEGUIDE TECHNIQUES FOR THE MEASUREMENT OF THE COMPLEX DIELECTRIC CONSTANTS OF SOLID MATERIALS, *ARRMS RF Microw. Soc.* (2002).
- [104] H. Qiao, K. Zhong, F. Li, X. Zhang, D. Xu, J. Yao, Temperature-Dependent Properties of Terahertz Window Materials, in: 2021 46th Int. Conf. Infrared Millim. Terahertz Waves IRMMW-THz, IEEE, Chengdu, China, 2021: pp. 1–2. <https://doi.org/10.1109/IRMMW-THz50926.2021.9567260>.
- [105] B.C. Wadell, *Transmission line design handbook*, Artech House Microwave Library, 1991.
- [106] J. Sun, S. Lucyszyn, Extracting Complex Dielectric Properties From Reflection-Transmission Mode Spectroscopy, *IEEE Access* 6 (2018) 8302–8321. <https://doi.org/10.1109/ACCESS.2018.2797698>.
- [107] R.I. Hunter, P.A.S. Cruickshank, D.R. Bolton, P.C. Riedi, G.M. Smith, High power pulsed dynamic nuclear polarisation at 94 GHz, *Phys. Chem. Chem. Phys.* 12 (2010) 5752–5756. <https://doi.org/10.1039/C002251A>.
- [108] A. Samoson, T. Tuherm, J. Past, A. Reinhold, T. Anupöld, I. Heinmaa, New Horizons for Magic-Angle Spinning NMR, in: J. Klinowski (Ed.), *New Tech. Solid-State NMR*, Springer Berlin Heidelberg, Berlin, Heidelberg, 2005: pp. 15–31. <https://doi.org/10.1007/b98647>.
- [109] N.C. Golota, Z.P. Fredin, D.P. Banks, D. Preiss, S. Bahri, P. Patil, W.K. Langford, C.L. Blackburn, E. Strand, B. Michael, B. Dastrup, K.A. Nelson, N. Gershenfeld, R. Griffin, Diamond Rotors, *J. Magn. Reson.* (2023) 107475. <https://doi.org/10.1016/j.jmr.2023.107475>.
- [110] St. Burghartz, B. Schulz, Thermophysical properties of sapphire, AlN and MgAl₂O₄ down to 70 K, *J. Nucl. Mater.* 212–215 (1994) 1065–1068. [https://doi.org/10.1016/0022-3115\(94\)90996-2](https://doi.org/10.1016/0022-3115(94)90996-2).
- [111] D.-M. Liu, C.-J. Chen, R.R.-R. Lee, Thermal diffusivity/conductivity in SiAlON ceramics, *J. Appl. Phys.* 77 (1995) 494–496. <https://doi.org/10.1063/1.359030>.
- [112] A. Franco Júnior, D.J. Shanafield, Thermal conductivity of polycrystalline aluminum nitride (AlN) ceramics, *Cerâmica* 50 (2004) 247–253. <https://doi.org/10.1590/S0366-69132004000300012>.
- [113] H.-S. Yang, G.-R. Bai, L.J. Thompson, J.A. Eastman, Interfacial thermal resistance in nanocrystalline yttria-stabilized zirconia, *Acta Mater.* 50 (2002) 2309–2317. [https://doi.org/10.1016/S1359-6454\(02\)00057-5](https://doi.org/10.1016/S1359-6454(02)00057-5).
- [114] A.B. Barnes, G. De Paëpe, P.C.A. van der Wel, K.-N. Hu, C.-G. Joo, V.S. Bajaj, M.L. Mak-Jurkauskas, J.R. Sirigiri, J. Herzfeld, R.J. Temkin, R.G. Griffin, High-Field Dynamic Nuclear Polarization for Solid and Solution Biological NMR, *Appl. Magn. Reson.* 34 (2008) 237–263. <https://doi.org/10.1007/s00723-008-0129-1>.
- [115] R. Harrabi, T. Halbritter, S. Alarab, S. Chatterjee, M. Wolska-Pietkiewicz, K.K. Damodaran, J. Van Tol, D. Lee, S. Paul, S. Hediger, S.Th. Sigurdsson, F. Mentink-Vigier, G. De Paëpe, AsymPol-TEKs as efficient polarizing agents for MAS-DNP in glass matrices of non-aqueous solvents, *Phys. Chem. Chem. Phys.* 26 (2024)

- 5669–5682.
<https://doi.org/10.1039/D3CP04271E>.
- [116] K.R. Thurber, R. Tycko, Perturbation of nuclear spin polarizations in solid state NMR of nitroxide-doped samples by magic-angle spinning without microwaves, *J. Chem. Phys.* 140 (2014) 184201. <https://doi.org/10.1063/1.4874341>.
- [117] C. Gabriel, S. Gabriel, E. H. Grant, E. H. Grant, B. S. J. Halstead, D. Michael P. Mingos, Dielectric parameters relevant to microwave dielectric heating, *Chem. Soc. Rev.* 27 (1998) 213. <https://doi.org/10.1039/a827213z>.
- [118] Y. Matsuki, T. Idehara, J. Fukazawa, T. Fujiwara, Advanced instrumentation for DNP-enhanced MAS NMR for higher magnetic fields and lower temperatures, *J. Magn. Reson.* 264 (2016) 107–115. <https://doi.org/10.1016/j.jmr.2016.01.022>.
- [119] R.E. Hummel, *Electronic Properties of Materials*, Springer Netherlands, Dordrecht, 1993. <https://doi.org/10.1007/978-94-017-4914-5>.
- [120] A.V. Inyushkin, A.N. Taldenkov, V.G. Ralchenko, A.P. Bolshakov, A.V. Koliadin, A.N. Katrusha, Thermal conductivity of high purity synthetic single crystal diamonds, *Phys. Rev. B* 97 (2018) 144305. <https://doi.org/10.1103/PhysRevB.97.144305>.
- [121] P. Goy, M. Gross, Free Space Vector Transmission-Reflection from 18 to 760 GHz, in: 1994 24th Eur. Microw. Conf., 1994: pp. 1973–1978. <https://doi.org/10.1109/EUMA.1994.337511>.
- [122] I. Farnan, H. Cho, W.J. Weber, R.D. Scheele, N.R. Johnson, A.E. Kozelisky, High-resolution solid-state nuclear magnetic resonance experiments on highly radioactive ceramics, *Rev. Sci. Instrum.* 75 (2004) 5232–5236. <https://doi.org/10.1063/1.1818512>.
- [123] J. Kischkat, S. Peters, B. Gruska, M. Semtsiv, M. Chashnikova, M. Klinkmüller, O. Fedosenko, S. Machulik, A. Aleksandrova, G. Monastyrskyi, Y. Flores, W. Ted Masselink, Mid-infrared optical properties of thin films of aluminum oxide, titanium dioxide, silicon dioxide, aluminum nitride, and silicon nitride, *Appl. Opt.* 51 (2012) 6789. <https://doi.org/10.1364/AO.51.006789>.
- [124] B.M. Fung, A.K. Khitrin, K. Ermolaev, An Improved Broadband Decoupling Sequence for Liquid Crystals and Solids, *J. Magn. Reson.* 142 (2000) 97–101. <https://doi.org/10.1006/jmre.1999.1896>.
- [125] A. Aitkenhead, Mesh Voxelization, MATLAB Central File Exchange, (2013).



- Dielectric properties of common materials used in high field DNP and EPR
- Characterization with quasi-optical bench between 70-960 GHz.
- Design of microwave efficient MAS rotors for DNP.
- Quantitative DNP simulations explain the field dependence of the Cross-Effect.

Journal Pre-proofs

Declaration of interests

The authors declare that they have no known competing financial interests or personal relationships that could have appeared to influence the work reported in this paper.

The authors declare the following financial interests/personal relationships which may be considered as potential competing interests: